# BIOCHEMISTRY
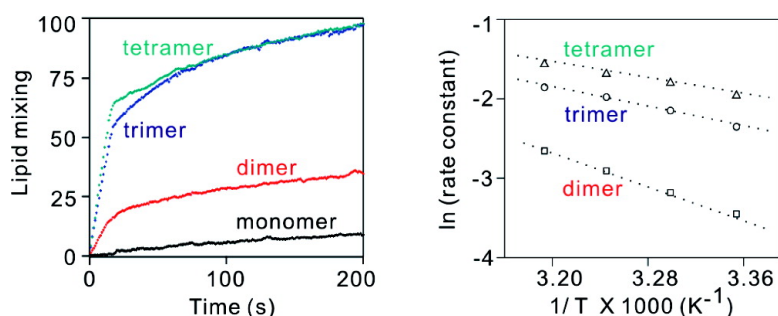including biophysical chemistry & molecular biology

Article

## HIV Fusion Peptide and Its Cross-Linked Oligomers: Efficient Syntheses, Significance of the Trimer in Fusion Activity, Correlation of # Strand Conformation with Membrane Cholesterol, and Proximity to Lipid Headgroups

Wei Qiang, and David P. Weliky

## More About This Article

Additional resources and features associated with this article are available within the HTML version:

- Supporting Information
- Access to high resolution figures
- Links to articles and content related to this article
- Copyright permission to reproduce figures and/or text from this article

View the Full Text HTML

## ACS Publications
High quality. High impact.

# HIV Fusion Peptide and Its Cross-Linked Oligomers: Efficient Syntheses, Significance of the Trimer in Fusion Activity, Correlation of $\beta$ Strand Conformation with Membrane Cholesterol, and Proximity to Lipid Headgroups[†]

Wei Qiang and David P. Weliky*

*Department of Chemistry, Michigan State University, East Lansing, Michigan 48824*

*Received August 19, 2008; Revised Manuscript Received November 12, 2008*

ABSTRACT: For enveloped viruses such as HIV, an ~20-residue N-terminal fusion peptide domain in the envelope protein binds to target cell membranes and plays a key role in fusion between the viral and cellular membranes during infection. The chemically synthesized HIV fusion peptide (HFP) catalyzes fusion between membrane vesicles and is a useful model system for understanding some aspects of HIV fusion. Previous studies have shown a common trimeric state for the envelope protein from several different viruses, including HIV, and in this study, practical high-yield syntheses are reported for HFP monomer (HFPmn) and chemically cross-linked HFP dimer (HFPdm), trimer (HFPtr), and tetramer (HFPte). The vesicle fusion rates per strand were ordered as follows: HFPmn < HFPdm < HFPtr ≈ HFPte. This suggested that HFPtr is the smallest catalytically efficient oligomer. Solid-state NMR measurements of $^{13}$CO chemical shifts were carried out in constructs labeled at either Ala-6 or Ala-15. For all constructs associated with cholesterol-containing membranes, the chemical shifts of both residues correlated with $\beta$ strand conformation while association with membranes without cholesterol resulted in a mixture of helical and $\beta$ strand conformations. The dependence of fusion rate on oligomer size is independent of membrane cholesterol content, so one interpretation of the data is fusion activity of both helical and $\beta$ strand conformations. Membrane location may be a determinant of fusion activity, and for all constructs in both conformations, a large fraction of the Ala-15 $^{13}$CO groups were 5−6 Å from the $^{31}$P atoms in the lipid headgroups, while the Ala-6 $^{13}$CO groups were more distant.

Infection by the human immunodeficiency virus (HIV)[1] begins with fusion between the viral and host cell membranes and leads to deposition of the viral nucleocapsid in the cytoplasm and viral replication (*1, 2*). The fusion process is mediated by the HIV gp41 fusion protein which contains a region inside HIV as well as a single-pass transmembrane domain. The ~170-residue ectodomain of gp41 lies outside HIV and is subdivided into a more C-terminal "soluble ectodomain" and an ~20-residue N-terminal fusion peptide (HFP) which is hydrophobic and fairly conserved. Peptides with the HFP sequence catalyze fusion between membrane vesicles, and there is good correlation between the mutation/fusion activity relationships of HFP-induced vesicle fusion and gp41-induced membrane fusion (*3−8*). These data suggest that studies of HFP will provide information about HIV−target cell fusion.

High-resolution structural studies have been carried out on the soluble ectodomain of gp41 which begins ~10 residues C-terminal of the HFP. These structures revealed trimeric oligomerization with the three N-termini in the proximity of each other (*1, 2, 9−11*). Trimeric oligomerization has also been observed in structures of fusion proteins from other "class I" enveloped viruses, including influenza virus (*1, 2*). These results have motivated study of oligomeric viral fusion peptides, including a HFP construct formed by cross-linking three HFPs at their C-termini to form a cross-linked HFP trimer (HFPtr) (*12−14*). The HFPtr construct induced vesicle fusion with a rate that was up to 40 times higher than the rate induced by non-cross-linked HFP monomer (HFPmn) (*13*). The rates were compared at a constant peptide strand:lipid molar ratio, i.e., 3 times less

[1] Abbreviations: au, arbitrary units; *d*, dipolar coupling; DCM, dichloromethane; DIPEA, *N,N*-diisopropylethylamine; DMAP, 4-(dimethylamino)pyridine; DMF, *N,N*-dimethylformamide; DMPC, 1,2-dimyristoyl-*sn*-glycero-3-phosphocholine; [$^{13}$C]DPPC, 1,2-dipalmitoyl-[1-$^{13}$C]-*sn*-glycero-3-phosphocholine; DTPC, 1,2-di-*O*-tetradecyl-*sn*-glycero-3-phosphocholine; DTPG, 1,2-di-*O*-tetradecyl-*sn*-glycero-3-[phospho-*rac*-(1-glycerol)]; Fmoc, 9-fluorenylmethoxycarbonyl; HBTU, *O*-benzotriazole-*N,N,N′,N′*-tetramethyluronium hexafluorophosphate; HEPES, *N*-(2-hydroxyethyl)piperazine-*N′*-2-ethanesulfonic acid; HFP, HIV fusion peptide; HFPdm, HFP dimer; HFPmn, HFP monomer; HFPte, HFP tetramer; HFPtr, HFP trimer; HIV, human immunodeficiency virus; HMB, *N*-2-hydroxy-4-methoxybenzyl; HOBT, 1-hydroxybenzotriazole; HPLC, high-performance liquid chromatography; LUVs, large unilamellar vesicles; MALDI-TOF, matrix-assisted laser desorption ionization time of-flight; MAS, magic angle spinning; NMR, nuclear magnetic resonance; *N*-NBD-PE, *N*-(7-nitro-2,1,3-benzoxadiazol-4-yl)phosphatidylethanolamine; *N*-Rh-PE, *N*-(lissamine rhodamine B sulfonyl)phosphatidylethanolamine; POPC, 1-palmitoyl-2-oleoyl-*sn*-glycero-3-phosphocholine; POPG, 1-palmitoyl-2-oleoyl-*sn*-glycero-3-[phospho-*rac*-(1-glycerol)]; PyAOP, 7-azabenzotriazol-1-yloxy tris(pyrrolidino)phosphonium hexafluorophosphate; REDOR, rotational-echo double-resonance; TFA, trifluoroacetic acid; TPPM, two-pulse phase modulation.

HFPtr than HFPmn, and suggested that the oligomeric topology enforced by C-terminal cross-linking is functionally important. The following questions remain. (1) Does the fusion rate per strand continue to increase for oligomers larger than the trimer? (2) Is there a structural basis for the increased fusion rate of cross-linked oligomers? This paper reports progress in answering both questions.

One experimental challenge in the study of cross-linked HFP oligomers has been production of large quantities of pure material. One synthetic route to HFPtr was cross-linking between HFPmn with one non-native C-terminal cysteine and HFPmn with two non-native C-terminal cysteines, but the major product was the HFP dimer (HFPdm) formed from cross-linking between the HFPmn with one cysteine (*12*). An alternative approach was initial formation of a peptide scaffold with three lysines and amide bonds between the ε-NH$_2$ group of the first lysine and the COOH group of the second lysine and between the ε-NH$_2$ group of the second lysine and the COOH group of the third lysine (*13*). HFPtr was then synthesized using standard 9-fluorenylmethoxy-carbonyl (Fmoc) chemistry and synchronous growth of the peptide chains from the three main chain α-NH$_2$ groups. This approach was therefore direct synthesis of an ∼90-mer, and the consequent yield was at best 5%. In addition, the final product contained significant impurity HFPtr which was nonseparable and which contained one additional lysine in one of the chains. This impurity was a consequence of undesired intramolecular removal of the Fmoc protecting group on a Lys α-NH$_2$ group by a free ε-NH$_2$ group (*15*).

This paper provides greatly improved approaches to syntheses of HFPmn, HFPdm, and HFPtr and a synthesis of the new HFP tetramer (HFPte). The residues in HFPmn and HFPdm which couple poorly to subsequent residues are identified, and conditions for improving yields are described. A much purer and higher yielding HFPtr synthesis is presented on the basis of cross-linking HFPmn and HFPdm which each contain a single cysteine. The paper also describes efficient chromatographic separation of HFPmn, HFPdm, HFPtr, and HFPte and quantitative comparison of the rates of vesicle fusion induced by the four constructs.

A separate section of the paper describes comparative solid-state nuclear magnetic resonance (NMR) structural studies of membrane-associated HFPmn, HFPdm, and HFPtr. In particular, the local conformations at the Ala-6 and Ala-15 residues were probed as well as the proximity of these residues to the lipid headgroups. These studies were motivated in part by hypotheses that the conformation and membrane location of HFP are significant structural factors which impact fusion catalysis and which might therefore explain the increased fusion rates of cross-linked HFP oligomers (*4, 16*).

The HFP structural literature is complex and includes liquid-state NMR studies in detergent micelles. For HFP: detergent molar ratios of ≤0.01, there is agreement that the residues between Ile-4 and Leu-12 form an uninterrupted α helix, and one study reports that the helix extends to Met-19 (*17−21*). A variety of biophysical techniques have been used to study the conformation of HFPmn associated with membranes (*5, 22*). Infrared spectra suggested that for a HFPmn:lipid ratio of 0.005 in membranes without cholesterol, a significant HFPmn fraction adopted helical structure while nonhelical structure was favored at higher ratios

(*23*). In addition, helical structure was favored with negatively charged lipids, while β strand structure was preferred with neutral lipids or with negatively charged lipids with bound Ca$^{2+}$ (*4, 16*). For membranes which have the approximate lipid headgroup and cholesterol composition of host cells of HIV, solid-state NMR studies have shown that HFPmn adopts an uninterrupted β strand conformation from Val-2 to Gly-16 with more disordered structure at Ala-21 (*24*). Small β sheet aggregates of HFPmn are formed under these conditions with predominant antiparallel alignment of adjacent peptides and adjacent strand crossing near Phe-8 and Leu-9. For this arrangement, most of the apolar 16-residue N-terminal region of HFPmn will form interpeptide hydrogen bonds which is biophysically reasonable because these residues are likely located in the membrane interior where there is little water available for hydrogen bonding. There is much less information about the structure of HFPdm and HFPtr. In membranes without cholesterol, predominant helical conformation was observed in HFPtr between Leu-7 and Phe-11, while in host cell-like membranes, β strand conformation was observed for HFPdm at Phe-8 and for HFPtr at Leu-7 and Phe-8 (*12−14*).

There is not yet a consensus about the location of HFPmn in either micelles or membranes. Data from liquid-state NMR experiments have supported either partial micelle insertion or micelle traversal with Ala-15 and Gly-16 at the micelle−solution boundary (*17−19*). Simulations of membrane-associated HFPmn have also been consistent with either partial membrane insertion or membrane traversal (*25, 26*). Fluorescence studies on membrane-associated HFP with the F8W mutation were consistent with a distance of ∼10 Å between the tryptophan indole group and the phosphorus longitude (*27, 28*). Electron spin resonance experiments have indicated that Met-19 is close to the membrane−water interface while Ala-1 is far from this interface (*29*).

Solid-state NMR has been applied to determine distances between backbone $^{13}$CO nuclei in HFPmn and $^{31}$P nuclei in the lipid headgroups (*30*). Because there was very little information about the membrane location of HFPmn, the initial experiments scanned the HFPmn backbone using samples with $^{13}$CO labeling at three sequential residues. A $^{13}$CO−$^{31}$P distance of 5−6 Å was observed for labeling between Ala-14 and Gly-16, while distances of >8 Å were observed for labeling between residues Gly-5 and Gly-13. The proximity of the Ala-14−Gly-16 region to headgroups in both micelles and membranes is very interesting because the HFPmn conformation is predominantly helical in micelles and β strand in membranes. To date, there have been no studies about the micelle or membrane locations of cross-linked HFP oligomers.

This solid-state NMR work uses HFPmn, HFPdm, and HFPtr which are labeled with $^{13}$CO at either Ala-6 or Ala-15 and examines samples in which there are both helical and β strand local conformations. Because the $^{13}$CO chemical shifts of helical and β strand Ala are well-resolved, the data provide information about the dependence of HFP membrane location on conformation as well as residue position. To the best of our knowledge, this is the first study of HFP membrane location for which HFP conformation is explicitly known.

Table 1: Names and Sequences of the HIV Fusion Peptides[a]

| Name | Sequence[b] |
|---|---|
| HFPmn | AVGIGALFLGFLGAAGSTMGARSWKKKKKKA[β] |
| HFPmn(Cys) | AVGIGALFLGFLGAAGSTMGARSWKKKKKCA[β] |
| HFPmn(Cys/Gly) | AVGIGALFLGFLGAAGSTMGARSWKKKKKCG |
| HFPdm(Cys) | AVGIGALFLGFLGAAGSTMGARSWKKKKKKA[β] <br> \| <br> AVGIGALFLGFLGAAGSTMGARSWKKKKKC |
| HFPdm | AVGIGALFLGFLGAAGSTMGARSWKKKKKCA[β] <br> \| <br> AVGIGALFLGFLGAAGSTMGARSWKKKKKCA[β] |
| HFPtr | AVGIGALFLGFLGAAGSTMGARSWKKKKKKA[β] <br> AVGIGALFLGFLGAAGSTMGARSWKKKKKC <br> \| <br> AVGIGALFLGFLGAAGSTMGARSWKKKKKCG |
| HFPte | AVGIGALFLGFLGAAGSTMGARSWKKKKKKA[β] <br> \| <br> AVGIGALFLGFLGAAGSTMGARSWKKKKKC <br> AVGIGALFLGFLGAAGSTMGARSWKKKKKC <br> \| <br> AVGIGALFLGFLGAAGSTMGARSWKKKKKKA[β] |

[a] The names of HFP samples labeled at $^{13}CO$ groups of A6 and A15 in the text are HFPmn-A6 and HFPmn-A15, respectively, etc. [b] A line between K and C denotes a peptide bond between the Cys CO group and the Lys $\varepsilon$-NH group, and a line between two C residues denotes a disulfide bond.

## MATERIALS AND METHODS

*Materials.* Resins and Fmoc-protected amino acids were purchased from Peptides International (Louisville, KY). $^{13}C$-carboxy-labeled amino acids were obtained from Cambridge Isotope Laboratories (Andover, MA) and were Fmoc-protected using literature methods (*31*). Lipids were obtained from Avanti (Alabaster, AL). Most other chemicals were obtained from Sigma-Aldrich (Milwaukee, WI). The most commonly used aqueous buffer contained 5 mM *N*-(2-hydroxyethyl)piperazine-*N'*-2-ethanesulfonic acid (HEPES) at pH 7.0 with 0.01% (w/v) NaN$_3$ preservative.

*Peptide Synthesis.* Table 1 displays the peptide constructs, and Figure 1 describes the synthetic schemes. Preloaded $\beta$-Ala Wang resin was often used because of its low level of substitution of ~0.2 mmol/g, and preloaded Gly Wang resin was also used. The non-native C-terminal lysines were introduced to increase the solubility of the peptides, and the non-native tryptophan provided a chromophore for quantification (*13*). The HFPmn constructs were made by linear synthesis. The HFPdm construct was made by cysteine cross-linking of HFPmn(Cys), and the HFPdm(Cys) construct was made from a dimer scaffold which included a peptide bond formed between the cysteine carboxyl group and a lysine $\varepsilon$-NH$_2$ group. The HFPtr construct was made by cysteine cross-linking of HFPdm(Cys) and HFPmn(Cys/Gly), and the HFPte construct was made by cysteine cross-linking of HFPdm(Cys).

Much of the synthesis was done manually in 5 mL polypropylene columns from Pierce (Rockford, IL), and mixing was accomplished with a rotation stage. Resin washing was done with *N,N*-dimethylformamide (DMF). Deprotection of the Fmoc group was done with two cycles of 20% piperidine in 3 mL, and deprotection of the Mtt group was done with six cycles of 1% trifluoroacetic acid (TFA) in 3 mL of dichloromethane (DCM). The first step in coupling of an amino acid to the $\alpha$-NH$_2$ terminus of the resin-bound peptide was dissolution in 4 mL of DMF of 0.5 mmol of protected amino acid, 0.5 mmol of *O*-benzotriazole-*N,N,N',N'*-tetramethyluronium hexafluorophosphate (HBTU), 0.5 mmol of 1-hydroxybenzotriazole (HOBT), and 1.0 mmol of *N,N*-diisopropylethylamine (DIPEA). After activation for 10 min, coupling was initiated by adding the amino acid solution to the resin. After coupling, acetylation or "capping" of unreacted peptides on the resin was accomplished with a 10 min reaction with a 3 mL solution containing acetic anhydride, pyridine, and DMF in a 2:1:3 volume ratio.

For HFPdm(Cys), the dimer scaffold was formed from coupling of the Cys COOH group to the $\varepsilon$-NH$_2$ group of the resin-bound Lys, and this step began with dissolution in 4 mL of DMF of 0.5 mmol of Fmoc-Cys(Trt), 0.5 mmol of 7-azabenzotriazol-1-yloxy tris(pyrrolidino)phosphonium hexafluorophosphate (PyAOP), and 1.0 mmol of DIPEA. The amino acid solution was transferred to the resin which had been washed twice with DCM and once with DMF after Mtt deprotection. One key aspect of this procedure was minimization of the time that the resin was at nonacidic pH prior to addition of the amino acid solution. This minimum time suppressed the undesired side reaction of deprotection of the Lys Fmoc group by the Lys $\varepsilon$-NH$_2$ group (*13, 15*).

For the HFPmn and HFPdm synthetic protocols, coupling at each residue was optimized by ninhydrin monitoring every 2 h to detect free $\alpha$-HN$_2$ groups (*32*). This information provided the basis for longer coupling times and double couplings at particular residues. Further explanation of the optimizations is provided in Results. Some of the HFPmn, HFPmn(Cys), and HFPmn(Cys/Gly) syntheses were conducted on an automated peptide synthesizer (ABI 431A, Applied Biosystems, Foster City, CA) using protocols similar to the ones described for manual synthesis. The automated synthesizer was also sometimes used for HFPdm(Cys) peptide elongation (Figure 1, step b).

Cross-linking reactions of HFPdm, HFPtr, and HFPte were conducted open to the atmosphere at pH 8.4 and were stopped by ~10-fold dilution with water and lyophilization. Further details are provided in the legend of Figure 1. For the NMR studies, single $^{13}C$-carbonyl ($^{13}CO$) labels were incorporated at either Ala-6 or Ala-15 in HFPmn, HFPdm, and HFPtr and the resultant peptides were denoted HFPmn-A6 or HFPmn-A15, respectively, etc.

Crude peptides were obtained by cleavage with a mixture of TFA, thioanisole, ethanedithiol, and anisole in a 90:5:3:2 volume ratio. The purification of crude peptides was completed by a HPLC system (Dionex, Sunnyvale, CA) equipped with a semipreparative C18 column (Vydac, Hesperia, CA). Buffer A was water with 0.1% TFA; buffer B was 90% acetonitrile, 10% water, and 0.1% TFA, and the gradient was from 40 to 80% buffer B over 30 min. Peptide masses were measured with MALDI-TOF mass spectroscopy using a Voyager-DE STR biospectrometry workstation (Applied Biosystems) and $\alpha$-cyano-4-hydroxycinnamic acid matrix. Peptide synthetic yields were quantified using 280 nm absorbance, and the extinction coefficients were 5700, 11600,
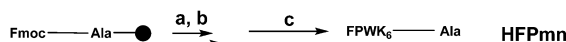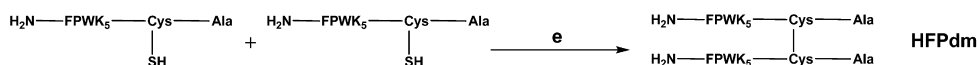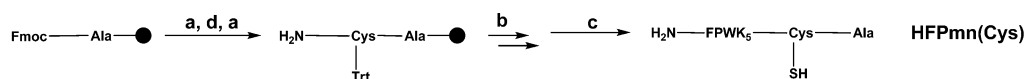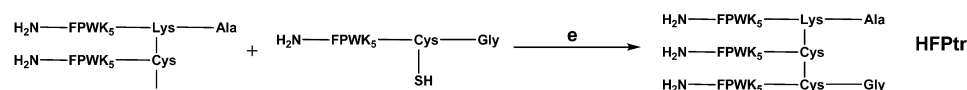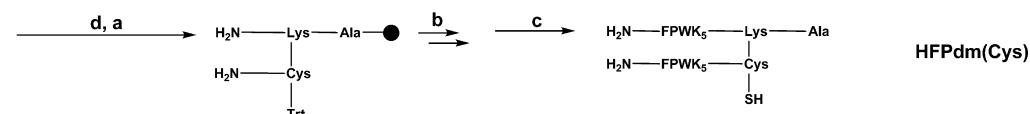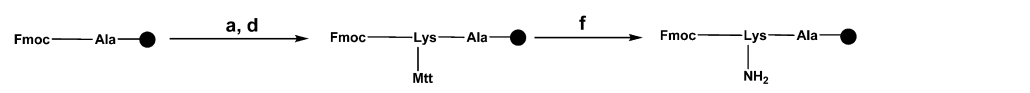
**Monomer Synthesis Scheme:**



**Dimer Synthesis Scheme:**



**Trimer Synthesis Scheme:**



**Tetramer Synthesis Scheme:**



FIGURE 1: Synthetic schemes of HFPmn, HFPdm, HFPtr, and HFPte. FP ≡ AVGIGALFLGFLGAAGSTMGARS. A black circle represents a resin bead. Lines are drawn to clarify chemical functionalities. An arrow signifies a chemical reaction. Two arrows signify multiple sequential chemical reactions. All reactions were carried out at ambient temperature. The specific reactions are as follows. Reaction a is Fmoc deprotection in 3 mL of 20% piperidine/DMF (v/v), at 15 min/cycle for two cycles. Reaction b is peptide synthesis with Fmoc chemistry. For HFPmn syntheses, 2 h single couplings were used for each amino acid with the following exceptions: 4 h single couplings for Trp, Ser, and Arg residues; 6 h single couplings for the Leu-12 to Leu-7 residues; and double coupling with 3 h per coupling for the $^{13}$CO-labeled residue. For the HFPdm(Cys) synthesis, 4 h single couplings were used for each amino acid with the following exceptions: 8 h single couplings for Trp, Ser, and Arg residues and double couplings with 4 h per coupling for the $^{13}$CO-labeled residue and for the Leu-12 to Leu-7 residues. Reaction c is cleavage from the resin using a 4 mL solution containing TFA, thioanisole, ethanedithiol, and anisole in a 90:5:3:2 volume ratio. After reaction for 2.5 h, TFA was removed with nitrogen gas and peptide was precipitated with cold methyl *tert*-butyl ether. Reaction d is coupling using PyAOP and DIPEA (1:2 molar ratio) in 4 mL of DMF with reaction times of 6 h for Cys and a reaction time of 2 h for Lys. Reaction e is cross-linking in 5 mM DMAP (pH 8.4), open to the air. HFPdm or HFPte conditions: 1 μmol of HFPmn(Cys) or HFPdm(Cys) in a 400 μL solution overnight. HFPtr conditions: 1 μmol of HFPmn(Cys) and 1.5 μmol of HFPdm(Cys) in a 400 μL solution for 2.5 h. Reaction f is selective deprotection of Mtt in 3 mL of 1% TFA/DCM (v/v), with 6 min/cycle for six cycles.

17300, and 23200 cm$^{-1}$ M$^{-1}$ for HFPmn, HFPdm, HFPtr, and HFPte, respectively.

*Lipid Mixing Induced by HFPs.* Mixing of lipids between membrane vesicles was monitored by a fluorescence assay (*33*). Two types of large unilamellar vesicles (LUVs) were prepared. The "unlabeled LUVs" contained 1-palmitoyl-2-oleoyl-*sn*-glycero-3-phosphocholine (POPC) and 1-palmitoyl-2-oleoyl-*sn*-glycero-3-[phospho-*rac*-(1-glycerol)] (POPG) in a 4:1 molar ratio. This composition approximately reflected the ratio of neutral to negatively charged lipids in membranes of host cells of HIV and correlated with the lipid composition used in previous structural studies of viral fusion peptides (*34, 35*). The "labeled LUVs" contained 77 mol % POPC, 19 mol % POPG, 2 mol % fluorescent lipid *N*-(7-nitro-2,1,3-benzoxadiazol-4-yl)phosphatidylethanolamine (*N*-NBD-PE), and 2 mol % quenching lipid *N*-(lissamine rhodamine B sulfonyl)phosphatidylethanolamine (*N*-Rh-PE). HFP-induced fusion was examined in a solution with an labeled:unlabeled vesicle ratio of 1:9 so that a labeled vesicle would likely fuse with an unlabeled vesicle. The resultant lipid mixing

would yield a larger average distance between fluorescent and quenching lipids and increased fluorescence.

Preparation of LUVs began with dissolution of lipid in chloroform followed by removal of the chloroform with nitrogen gas and overnight vacuum pumping. The lipid film was suspended in 5 mM HEPES buffer, and the lipid dispersion was homogenized with 10 freeze−thaw cycles. LUVs were formed by extrusion through a filter with 100 nm diameter pores (Avestin, Ottawa, ON).

Fluorescence was recorded on a stopped-flow fluorimeter (model SX.18MV-R, Applied Photophysics, Surrey, U.K.) using excitation and emission wavelengths of 465 and 530 nm, respectively. For a single run, one syringe in the fluorimeter contained HFPmn, HFPdm, HFPtr, or HFPte dissolved at a concentration of 3.00, 1.50, 1.00, or 0.75 μM in HEPES buffer, respectively. A second syringe contained labeled and unlabeled LUVs at a total lipid concentration of 300 μM. At time zero, equal volumes of the two solutions were mixed and fluorescence was recorded every second for

200 s. The HFP concentrations were chosen so that the HFP strand:lipid ratio was always 0.010.

Most reports of fluorescence-based lipid mixing have focused on $\Delta F_{\text{fusogen}}$, the net change in fluorescence after the fusogen is added to the vesicles. $\Delta F_{\text{fusogen}}$ is typically compared to $\Delta F_{\text{detergent}}$, the change caused by addition of a detergent which completely solubilizes the vesicles. Because of the very large average distance between fluorescent and quenching lipids in the solubilized vesicles, $\Delta F_{\text{detergent}}$ is the maximum observable fluorescence change. The "percent lipid mixing" is typically defined as $\Delta F_{\text{fusogen}}/\Delta F_{\text{detergent}} \times 100$. To provide some comparison between our stopped-flow fluorescence data and the lipid mixing literature, the raw data at each time point, $F_{\text{raw}}(t)$, were converted to normalized $F(t)$:

$$F(t) = \{[F_{\text{raw}}(t) - F_{\text{initial}}]/\Delta F_{\text{max}}\} \times 100 \quad (1)$$

$F_{\text{initial}}$ was a typical value of fluorescence at time zero, and $\Delta F_{\text{max}}$ was chosen to provide semiquantitative comparison between $F(t)$ and earlier studies of percent lipid mixing induced by HFPs (12). A single value of $F_{\text{initial}}$ and a single value of $\Delta F_{\text{max}}$ were used for all of the data.

At the end of the 200 s collection time, the fluorescence from HFPmn-induced lipid mixing was still appreciably increasing, and it was therefore difficult to fit these data to a buildup function. The fluorescence of the HFPdm, HFPtr, and HFPte constructs had leveled off, and these data fitted much better to the sum of two exponential buildup functions than to a single buildup function:

$$F(t) = F_0 + F_1(1 - e^{-k_1 t}) + F_2(1 - e^{-k_2 t}) \quad (2)$$

where $F_0$, $k_1$, $F_1$, $k_2$, and $F_2$ were fitting parameters. The best-fit value of $F_0$ was close to 0 because of the way $F(t)$ was calculated in eq 1. A convention was chosen that $k_1 > k_2$ so that $k_1$ and $F_1$ were the rate constant and overall fluorescence change, respectively, of the faster lipid mixing process and $k_2$ and $F_2$ were the rate constant and overall fluorescence change, respectively, of the slow process.

Data were collected for each construct at 25, 30, 35, and 40 °C, and each HFPdm, HFPtr, and HFPte data set was fitted with eq 2. For each construct, the temperature dependence of $k_1$ was fitted to the Arrhenius equation $\ln k_1 = \ln A - E_a/RT$, where $R$ is the ideal gas constant, $T$ is the absolute temperature, and $A$ and $E_a$ are the pre-exponential factor and activation energy, respectively. Three independent runs were conducted for each construct and temperature.

*Preparation of Solid-State NMR Samples.* The membrane lipids were 1,2-di-*O*-tetradecyl-*sn*-glycero-3-phosphocholine (DTPC) and 1,2-di-*O*-tetradecyl-*sn*-glycero-3-[phospho-*rac*-(1-glycerol)] (DTPG). For each HFP construct, one sample was made with a 4:1 DTPC:DTPG or "PC:PG" ratio and the other with an 8:2:5 DTPC:DTPG:cholesterol or "PC:PG:CHOL" ratio. The lipid:cholesterol ratio of PC:PG:CHOL correlated with the ratio found in membranes of cells infected with HIV (34, 35). DTPC and DTPG were used because they were ether-linked rather than ester-linked lipids and thus lacked natural abundance $^{13}$CO NMR signals. Spectral interpretation was therefore simplified because the $^{13}$CO region of the NMR spectrum was dominated by the labeled $^{13}$CO nucleus of the HFP. For membrane-associated HFPtr, a previous study showed that the Leu-7 $^{13}$CO chemical shift

and presumably the Leu-7 local conformation were similar in membranes containing either ether-linked or ester-linked lipids (14).

Each PC/PG sample contained 16 μmol of DTPC and 4 μmol of DTPG, and each PC/PG/CHOL sample contained 16 μmol of DTPC, 4 μmol of DTPG, and 10 μmol of cholesterol. Sample preparation began with creation of LUVs in 2 mL of HEPES buffer using the protocol described in the previous section. Either HFPmn (0.80 μmol), HFPdm (0.40 μmol), or HFPtr (0.27 μmol) was dissolved in 2 mL of HEPES buffer, and the HFP and vesicle solutions were then mixed and gently vortexed together with a resulting HFP strand:lipid ratio of 0.040 for all samples. The mixture was refrigerated overnight and ultracentrifuged at ~150000g for 5 h. Unbound HFPs do not pellet, and at least HFPmn binding to membranes has been determined to be approximately quantitative (13, 36). The membrane pellet with associated bound HFP was transferred to a 4 mm diameter magic angle spinning (MAS) NMR rotor.

*Solid-State NMR REDOR Experiments and Data Analysis.* The evolution of $^{13}$CO magnetization under the effect of $^{13}$CO−$^{31}$P dipolar coupling was measured with solid-state NMR rotational-echo double-resonance (REDOR) experiments. The REDOR pulse sequence contained in sequence (1) a 50 kHz $^1$H π/2 pulse, (2) 1 ms cross-polarization with a 52 kHz $^1$H field and a 58−69 kHz ramped $^{13}$C field, (3) a dephasing period τ which contained ~50 kHz $^{13}$C π and in some cases ~60 kHz $^{31}$P π pulses with XY-8 phase cycling on each channel, and (4) $^{13}$C detection (14, 37). Two-pulse phase modulation (TPPM) $^1$H decoupling with a 100 kHz Rabi frequency was applied during the dephasing and detection periods. For each sample and each τ, two spectra were acquired. The dephasing period in the "$S_1$" acquisition contained a $^{13}$C π pulse at the end of each rotor cycle except for the last cycle and a $^{31}$P π pulse in the middle of each cycle. There were no $^{31}$P π pulses in the "$S_0$" acquisition. MAS averaged the $^{13}$C evolution due to $^{13}$C−$^{31}$P dipolar coupling to zero over each rotor period of the $S_0$ acquisition, while the two π pulses in each rotor cycle of the $S_1$ acquisition disrupted the averaging and resulted in a net dipolar coupling "$d$" with consequent reduction of the $^{13}$C signal. Determination of $d$ was based on the difference of $^{13}$C intensity between the $S_0$ and $S_1$ spectra. For a single $^{13}$CO−$^{31}$P spin pair, the $^{13}$CO−$^{31}$P distance "$r$" in angstroms is related to $d$ in hertz by the relationship $r = 23.05/d^{1/3}$. Further details are provided in the Supporting Information.

## RESULTS

*Peptide Synthesis.* Table 1 summarizes the HFPmn, HFPdm, HFPtr, and HFPte constructs synthesized in this study, and Figure 1 shows the synthetic schemes. A manual synthesis was carried out on HFPmn, and the efficiency after each coupling was monitored with the ninhydrin test. A 2 h single coupling was not sufficient for the Ser, Arg, and Trp residues or for the residues between Leu-12 and Leu-7, and the optimized synthesis used longer coupling times or double coupling for these residues. Figure 2a displays the HPLC chromatogram of an optimized HFPmn synthesis. The mass spectrum of the dominant fraction had an intense peak with an ion at *m*/*z* 3149 Da which was very close to the expected value of *m*/*z* 3151 Da for HFPmn (cf. Figure 2b). The
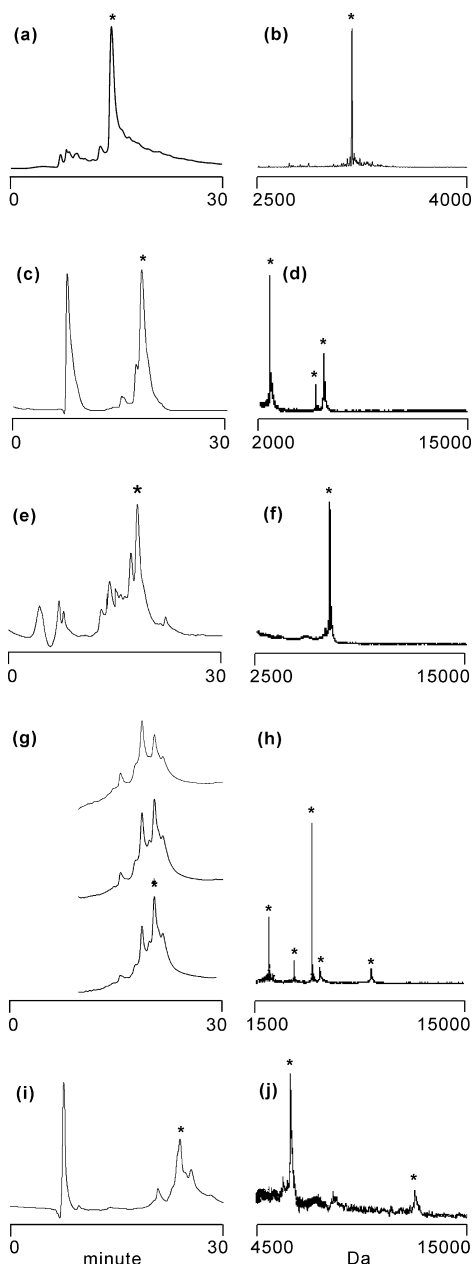
FIGURE 2: (a, c, e, g, and i) HPLC chromatograms obtained during peptide purification correspond to the following syntheses: (a) HFPmn, (c) HFPdm, (e) HFPdm(Cys), (g) HFPtr, and (i) HFPte. The top, middle, and bottom chromatograms in panel g are for syntheses with HFPtr cross-linking times of 0.5, 1.5, and 2.5 h, respectively. The vertical scales in panels a, c, e, and i are $A_{214}$, and the vertical scale in panel g is $A_{280}$. In panels c and i, the large peaks at 8 min are due to DMAP. For a given chromatogram in the left column, the HPLC fraction marked with an asterisk was analyzed by MALDI-TOF mass spectroscopy and the corresponding mass spectrum is displayed in the right column. The spectral peaks marked with asterisks are discussed in the text.

HFPmn(Cys) synthesis was carried out under the same conditions and had a very similar chromatogram, and the mass spectrum of the dominant fraction had an ion at $m/z$ 3125 Da which was very close to the expected value of $m/z$ 3126 Da of HFPmn(Cys).

HFPdm was made by cross-linking HFPmn(Cys), and the HPLC retention time of HFPdm was very well-separated from that of unreacted HFPmn(Cys) (cf. Figure 2c). The HFPdm fraction had a mass spectral peak at $m/z$ 6248 Da which was very close to the expected value of $m/z$ 6153 Da

(cf. Figure 2d). There was also a peak at $m/z$ 3124 Da which corresponded to either the HFPmn(Cys) fragment formed from cleavage of the disulfide bond in the mass spectrometer or doubly charged HFPdm. The insulin standard at 5734 Da was also apparent. Ninhydrin monitoring of the manual synthesis of HFPdm(Cys) showed that the difficult coupling steps were the same as those of the HFPmn synthesis, and the optimized synthesis included longer and/or double couplings. Figure 2e displays the chromatogram of the synthesis, and the retention time of HFPdm(Cys) was very close to that of HFPdm. The mass spectrum of the HFPdm(Cys) fraction had an intense peak at $m/z$ 6190 Da which was very close to the expected peak at $m/z$ 6188 Da (cf. Figure 2f). A previously published synthesis showed significant higher-molecular weight impurities which were the result of (1) premature removal of the scaffold lysine Fmoc group by nucleophilic attack of the scaffold lysine $\varepsilon$-NH$_2$ group and (2) subsequent coupling of the next amino acid with both the $\varepsilon$- and the $\alpha$-NH$_2$ groups of the scaffold lysine (*13*). The mass spectrum of HFPdm(Cys) did not show the impurity corresponding to a peptide with an extra Cys. Minimization of the time between steps f and d in Figure 1 was critical to eliminating this impurity.

HFPtr was formed from cross-linking HFPmn(Cys) and HFPdm(Cys) in a 1.0:1.5 molar ratio. The nonstoichiometric ratio was based on initial small-scale syntheses which showed that cross-linking of HFPmn(Cys) with itself to form HFPdm was more rapid than cross-linking of HFPmn(Cys) with HFPdm(Cys) to form HFPtr. The top chromatogram in Figure 2g was obtained after cross-linking for 0.5 h, and the three prominent peaks from left to right were HFPmn, HFPdm, and HFPtr, respectively. The middle and bottom chromatograms were obtained with cross-linking times of 1.5 and 2.5 h, respectively, and showed a relative increase in the level of HFPtr and relative decreases in the levels of HFPmn(Cys) and HFPdm(Cys) with longer cross-linking times. The mass spectrum of the HFPtr fraction had a peak at $m/z$ 9307 Da which was close to the expected HFPtr peak at $m/z$ 9312 Da (cf. Figure 2h). The peak at 4653 Da was assigned to doubly charged HFPtr, and the peaks at 3112 and 6194 Da were assigned to HFPmn(Cys) and HFPdm(Cys) fragments, respectively, formed from cleavage of the disulfide bond in the mass spectrometer. The insulin standard at 5734 Da was also apparent. HFPte was formed from cross-linking HFPdm(Cys), and the chromatogram exhibited good separation of the HFPte and unreacted HFPdm(Cys) fractions (cf. Figure 2i). Relative to the mass spectra of HFPmn, HFPdm, and HFPtr, the mass spectrum of the HFPte fraction had a lower signal-to-noise ratio (cf. Figure 2j). There were broad signals that peaked at $m/z$ 12461 and 6235 Da which were comparable to the expected HFPte peak at $m/z$ 12374 Da and the $m/z$ value of the doubly charged species or the HFPdm(Cys) fragment, respectively, formed from cleavage of the disulfide bond in the mass spectrometer. Relative to the HFPmn, HFPdm, and HFPtr spectra, there were greater uncertainties of the experimental $m/z$ values in the HFPte spectra because of both broader signals and a lower signal-to-noise ratio.

*Lipid Mixing.* Figure 3a shows stopped-flow fluorescence data which track lipid mixing induced by HFPs. Both HFPtr and HFPte induced similar rapid lipid mixing, while HFPdm induced slower mixing and HFPmn little mixing. For each
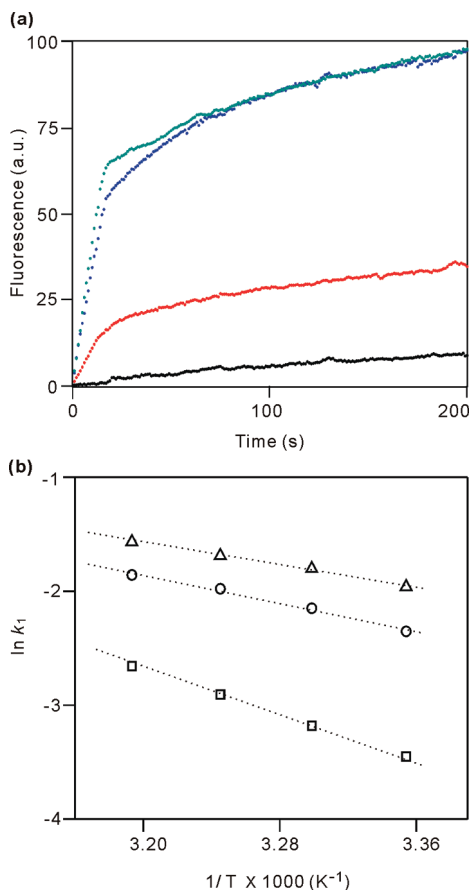
FIGURE 3: (a) Stopped-flow-monitored changes in lipid fluorescence induced by addition of different HFP constructs to an aqueous solution containing membrane vesicles. Increased fluorescence is a result of mixing of lipids between different vesicles, and this mixing is one consequence of vesicle fusion. The lines are color-coded: black for HFPmn, red for HFPdm, blue for HFPtr, and green for HFPte. The total lipid concentration was 150 $\mu$M, and the HFPmn, HFPdm, HFPtr, and HFPte concentrations were 1.50, 0.75, 0.50, and 0.37 $\mu$M, respectively, so that the peptide strand:lipid ratio was 0.01. The data were collected at 25 °C; the vesicle composition was 4:1 POPC:POPG, and the initial vesicle diameter was ~100 nm. Additional data (not shown) were obtained for HFPdm, HFPtr, and HFPte at 30, 35, and 40 °C. Each data set for each construct was analyzed as the sum of two exponential buildup functions. Panel b displays Arrhenius plots for the rate constants of the fast buildup function: ($\square$) HFPdm, ($\bigcirc$) HFPtr, and ($\triangle$) HFPte. The best-fit lines are also displayed and result in activation energies of 41 ± 3, 26 ± 1, and 20 ± 1 kJ/mol, respectively.

construct, data were acquired at 25, 30, 35, and 40 °C, and the HFPdm, HFPtr, and HFPte data could be fit well to a biexponential buildup function (cf. eq 2). The best-fit parameters of the 35 °C data are listed in Table 2, and the parameters for other temperatures are listed in the tables in the Supporting Information. For each of the three constructs, $k_2 \approx 0.1k_1$ and $F_1 \approx F_2$. In addition, $k_1^{tr}/k_1^{dm} \approx 2.5$ and $k_1^{te}/k_1^{tr} \approx 1.3$. Figure 3b displays Arrhenius plots for the $k_1$ rate constants, and the best-fit $E_a$ values and ln $A$ values are listed in Table 2. The values of $E_a$ and ln $A$ for HFPdm and HFPtr are comparable to those reported in a previous study (13). The data show that $E_a^{dm} > E_a^{tr} > E_a^{te}$ and ln $A_{dm} >$ ln $A_{tr} >$ ln $A_{te}$. An increased number of strands in the oligomer is therefore correlated with a decreased ln $A$ and $E_a$ with concomitant opposite effects on $k_1$. The activation entropies were calculated using the transition-state theory equation $\Delta S^{\ddagger} = R[\ln(Ah/k_B T) - 2]$, where $R$ is the ideal gas constant, $h$ is

Planck's constant, $k_B$ is Boltzmann's constant, and $T$ is the absolute temperature (13). The resultant $\Delta S^{\ddagger}$ values were all negative ($\Delta S^{\ddagger}_{dm} > \Delta S^{\ddagger}_{tr} > \Delta S^{\ddagger}_{te}$), but we do not understand the sign or trends of the $\Delta S^{\ddagger}$ values.

*Solid-State NMR.* Figure 4a displays the $^{13}$CO $S_0$ and $S_1$ REDOR spectra at $\tau = 24$ ms for the PC/PG membrane-associated HFP-A6 samples. The line shapes of the $S_0$ spectra did not exhibit a strong dependence on dephasing time, and the displayed spectra were therefore representative of the $^{13}$CO shift distributions of the samples. The $^{13}$CO $S_0$ signal had an approximately three-fourths contribution from the labeled Ala-6 and an approximately one-fourth natural abundance contribution from the unlabeled residues. Because the latter contribution was due to ~29 chemically distinct $^{13}$CO groups, it would be a broad signal and therefore less apparent than the sharper $^{13}$CO signals from the single labeled residue. In each spectrum, there are two peaks with chemical shifts of ~180 and ~175 ppm which likely have dominant contributions from separate populations of helical and $\beta$ strand Ala-6 conformations (38). This correlation of $^{13}$CO chemical shift with conformation was previously confirmed with backbone $^{13}$CO$-^{15}$N distance measurements on HFPtr (14). For PC/PG/CHOL membrane-associated HFP-A6 samples, the 175 ppm peak is dominant and is consistent with a preference for $\beta$ strand conformation in cholesterol-containing membranes (cf. Figure 4b). The correlation holds for all three constructs.

Figure 4c displays a plot of $(\Delta S/S_0)^{exp}$ versus dephasing time for the helical component of the PC/PG membrane-associated HFP-A6 samples, and Figure 4d displays the corresponding plot for the PC/PG/CHOL samples in which the $\beta$ strand conformation is dominant. In Figure 4d, $(\Delta S/S_0)^{exp} \approx 0$ for all $\tau$ values and all constructs, and this was also true for the $\beta$ strand component in the PC/PG samples (not shown). This result is consistent with Ala-6 $^{13}$CO$-^{31}$P distances greater than 8 Å. For the helical component of HFPtr, $(\Delta S/S_0)^{exp} \approx 0$ for all $\tau$ values; for HFPdm, there was a small increase with an increase in $\tau$, and for HFPmn, a larger increase which leveled off at 0.2 at large $\tau$ values was observed. These data support an Ala-6 membrane location which is closest to the lipid $^{31}$P atoms in HFPmn, more distant in HFPdm, and most distant in HFPtr. For the helical conformation, there may therefore be a positive correlation between the number of strands in the oligomer and the depth of membrane insertion. This variation in membrane location may be one reason for the large differences in fusion rates among the different constructs.

Figure 5 displays the $^{13}$CO $S_0$ and $S_1$ REDOR spectra at $\tau = 24$ ms for the (a) PC/PG membrane- and (b) PC/PG/CHOL membrane-associated HFP-A15 samples. In the PC/PG samples, the peak $^{13}$CO shift was ~178 ppm, and at least for HFPtr, there was also a clear shoulder at ~176 ppm; in the PC/PG/CHOL samples, the peak $^{13}$CO shift was ~176 ppm. These shifts generally correlate with a mixture of helical and $\beta$ strand conformations for Ala-15 in PC/PG samples and predominant $\beta$ strand conformation in PC/PG/CHOL samples. This result is consistent with the Ala-6 data. The line widths of components of individual Ala-15 conformations are significantly broader than the corresponding components of Ala-6 conformations, which is consistent with greater structural heterogeneity at Ala-15 (cf. Figures 4b and 5b).

Table 2: Fitting Parameters for the Lipid Mixing Kinetics at 35 °C[a]

| construct | $k_1$ ($\times 10^{-3}$ s$^{-1}$) | $k_2$ ($\times 10^{-3}$ s$^{-1}$) | $F_0$ (au) | $F_1$ (au) | $F_2$ (au) | $E_a^b$ (kJ/mol) | ln $A$ | $\Delta S^{\ddagger c}$ (J mol$^{-1}$ K$^{-1}$) |
|---|---|---|---|---|---|---|---|---|
| HFPdm | 54.9 (0.3) | 4.9 (0.2) | 0.5 (0.1) | 19.6 (0.3) | 19.8 (0.1) | 40.6 (3.4) | 13.2 (1.2) | −152 |
| HFPtr | 139 (3) | 17.3 (0.3) | 0.9 (0.2) | 50.1 (0.2) | 50.0 (0.2) | 25.8 (1.2) | 8.0 (0.8) | −195 |
| HFPte | 185 (7) | 20.7 (0.3) | 0.9 (0.3) | 49.8 (0.2) | 50.1 (0.2) | 20.1 (0.7) | 6.2 (0.5) | −210 |

[a] Fitting uncertainties are given in parentheses. The variation of a parameter value from fitting data of different runs was less than the fitting uncertainty of a single run. The $k_1$, $k_2$, $F_0$, $F_1$, and $F_2$ were obtained using eq 2 in the text. [b] $E_a$ and ln $A$ were calculated using ln $k_1 = \ln A - E_a / RT$ and $k_1$ values from temperatures between 25 and 40 °C. [c] $\Delta S^{\ddagger}$ was calculated using the relation $\Delta S^{\ddagger} = R[\ln(Ah/k_B T) - 2]$.

Figure 5c displays the plot of $(\Delta S/S_0)^{\text{exp}}$ versus $\tau$ for the PC/PG membrane-associated HFP-A15 samples, and Figure 5d displays the corresponding plot for the PC/PG/CHOL membrane-associated samples. The $(\Delta S/S_0)^{\text{exp}}$ values were derived from 1 ppm integration windows at the peak shifts and therefore reflect helical and $\beta$ strand conformations in the respective samples. For all constructs and all conformations, there was a large increase in $(\Delta S/S_0)^{\text{exp}}$ with an increase in $\tau$ and the $(\Delta S/S_0)^{\text{exp}}$ values were generally much larger than for the HFP-A6 samples. These data support a membrane location for Ala-15 which is much closer to the lipid $^{31}$P atoms than is Ala-6.

*Quantitative Analysis of $^{13}C-^{31}P$ REDOR Data.* A more quantitative analysis of the REDOR data was carried out for the HFP-A15 samples. The analysis included approximate separation of the natural abundance contribution from the labeled contribution to $(\Delta S/S_0)^{\text{exp}}$, so that the resultant $(\Delta S/S_0)^{\text{lab}}$ reflected the Ala-15 $^{13}CO-^{31}P$ proximity. The $(\Delta S/S_0)^{\text{lab}}/(\Delta S/S_0)^{\text{exp}}$ ratio varied with $\tau$ with a typical range of 0.9−1.2, so a plot of $(\Delta S/S_0)^{\text{lab}}$ versus $\tau$ was similar to the corresponding plot of $(\Delta S/S_0)^{\text{exp}}$ versus $\tau$. As inferred from panels c and d of Figure 5, there was a plateau value of $(\Delta S/S_0)^{\text{lab}}$ in each data set which was between 0.3 and 0.4, and it was therefore considered that only a fraction $f$ of the Ala-15 $^{13}CO$ groups had detectable $d$. This plateau effect had also been observed in fitting $^{13}CO-^{31}P$ data of a membrane-associated antimicrobial peptide with a helical conformation (37). The Supporting Information contains further information and details about the natural abundance correction, calculation of $(\Delta S/S_0)^{\text{sim}}$ values as a function of $d$, and fitting of $(\Delta S/S_0)^{\text{lab}}$ to $(\Delta S/S_0)^{\text{sim}}$ to determine best-fit $d$ and $f$ values.

Table 3 summarizes the best-fit $d$ and $f$ values for the three constructs in the two different compositions and conformations. The calculation of $(\Delta S/S_0)^{\text{sim}}$ as a function of $d$ was based on a single nearby $^{31}P$ nucleus. All of the $d$ values were in the range of 60−90 Hz which correspond to $^{13}CO-^{31}P$ distances in the 5−6 Å range, and all of the $f$ values were in the range of 0.3−0.4. Because the HFP $^{13}CO$ group may be close to more than one lipid headgroup, fittings were also done using simulations with one $^{13}CO$ and two $^{31}P$ spins and resulted in best-fit $^{13}CO-^{31}P$ distances of 5−6 Å, $f$ values of 0.6−0.8, and an angle between the two $^{13}CO-^{31}P$ vectors close to 180° (14, 39, 40). For this angle, $(\Delta S/S_0)^{\text{sim}} \approx 0.5$ at long dephasing times. There is insufficient information to choose between the one- and two-$^{31}P$ spin models.

## DISCUSSION

This work describes syntheses, fusion activities, conformations, and membrane locations of four HFP constructs, including the HFPmn monomer and the HFdm, HFPtr, and

HFPte cross-linked oligomers that are dimeric, trimeric, and tetrameric, respectively. The putative oligomerization state of HIV gp41 is a trimer, and motivations for our studies included understanding the role of oligomerization in the HFP model system and providing insight into the role of oligomerization in intact HIV−host cell fusion.

One result of this work is an improved synthesis of HFPtr and the synthesis of HFPte. The previous synthetic strategy for HFPtr used a trimeric scaffold and simultaneous coupling of amino acids onto each chain of the scaffold (13). This approach often led to synthetic failure because of the requirement for ∼180 successful deprotection and coupling reactions. In addition, use of a 4 h coupling time for all residues did not consider inefficient coupling for residues that contained large side chains or side chain protecting groups. This study increased the HFPtr yield and purity using the following modifications. (1) HFPtr was formed from a cysteine cross-linking reaction between HFPmn(Cys) and HFPdm(Cys). Because HFPdm(Cys) was synthesized using a dimeric scaffold, a successful synthesis required one-third fewer reactions than the earlier HFPtr synthesis. In addition, the purification of the cross-linking reaction was fairly straightforward because of the separation of the HPLC peaks corresponding to HFPmn(Cys), HFPdm and HFPdm(Cys), HFPtr, and HFPte (cf. Figure 2g). (2) Ninhydrin monitoring of coupling reactions in the manual syntheses of HFPmn and HFPdm(Cys) showed that longer coupling times were required for the Trp, Ser, Arg, and Leu-12−Leu-7 residues. The new synthetic protocol used longer coupling times or double coupling at these residues. (3) The HFPdm(Cys) synthetic protocol was modified to minimize the time between the cleavage of the Mtt group of the Lys $\varepsilon$-NH$_2$ group and the subsequent coupling to Cys. This modification reduced the level of undesired deprotection of the Fmoc group of the Lys $\alpha$-NH$_2$ group by the $\varepsilon$-NH$_2$ group (15).

The lipid mixing at long times was ordered as follows: HFPmn < HFPdm < HFPtr ≈ HFPte (cf. Figure 3a). $k_1^{\text{HFPtr}}/k_1^{\text{HFPdm}} \approx 2.5$, while $k_1^{\text{HFPte}}/k_1^{\text{HFPtr}} \approx 1.3$ (cf. Table 2), where $k_1$ is the rate constant of the fast component of lipid mixing. In addition, $E_a^{\text{HFPdm}} - E_a^{\text{HFPtr}} \approx 15$ kJ/mol whereas $E_a^{\text{HFPtr}} - E_a^{\text{HFPte}} \approx 6$ kJ/mol. These data indicate (1) the fact that cross-linking increases the rate and extent of HFP-induced lipid mixing and decreases the activation energy and (2) the increase in the level of lipid mixing per strand and decrease in activation energy with cross-linking levels off at HFPtr. It might be expected that oligomer folding would be more difficult with an increasing number of monomer units, so the putative trimeric oligomerization state of gp41 and other class I viral fusion proteins may be the optimal balance between higher catalytic efficiency and more difficult folding. We do not know why lipid mixing appears to be a combination of a fast ($k_1$) and slow ($k_2$) processes.
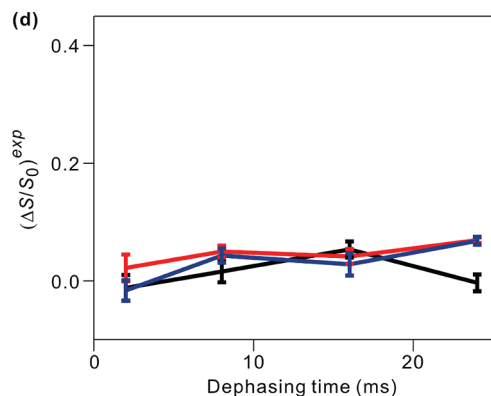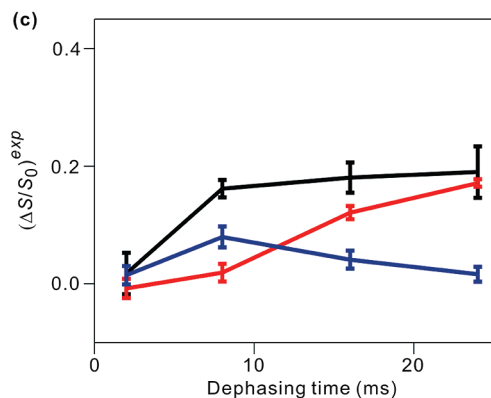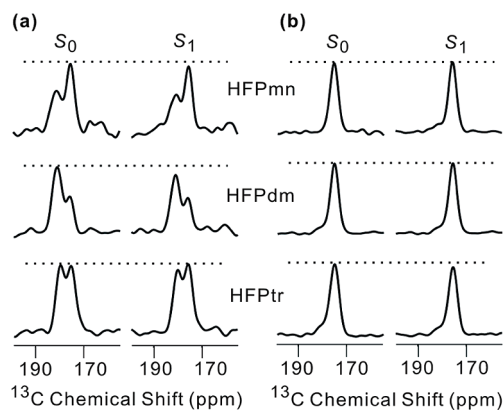
FIGURE 4: (a) $^{13}$C-detect/$^{31}$P-dephase REDOR $S_0$ and $S_1$ spectra for PC/PG membrane-associated HFPs and (b) spectra for PC/PG/CHOL membrane-associated HFPs. The dotted lines are added to provide easier visual comparison of the $S_0$ and $S_1$ intensities. The samples for the top, middle, and bottom spectra contained HFPmn-A6, HFPdm-A6, and HFPtr-A6, respectively, and the HFP:lipid molar ratios were 0.040, 0.020, and 0.013, respectively. Each spectrum was obtained with a dephasing time of 24 ms and was processed with 300 Hz Gaussian line broadening and polynomial baseline correction. For panel a, the numbers of scans summed for each $S_0$ and $S_1$ spectrum were 40832 for HFPmn-A6, 74756 forHFPdm-A6, and 20736 for HFPtr-A6. For panel b, the numbers of scans were 28288 for HFPmn-A6, 85136 for HFPdm-A6, and 29696 for HFPtr-A6. Panels c and d display plots of $(\Delta S/S_0)^{exp}$ vs dephasing time with color coding: black for HFPmn, red for HFPdm, and blue for HFPtr. A 1$\sigma$ error bar is displayed for each point, and lines between points are displayed for visual clarity. Each $(\Delta S/S_0)^{exp}$ value was determined from integrations of 1 ppm regions of the $S_0$ and $S_1$ spectra. In the panel c plot, the integration was centered at the ~180 ppm peak for samples containing PC and PG, and for the panel d plot, the integration was centered at the ~175 ppm peak for samples containing PC, PG, and CHOL. These two peaks are assigned to helical and $\beta$ strand A6 conformations, respectively.
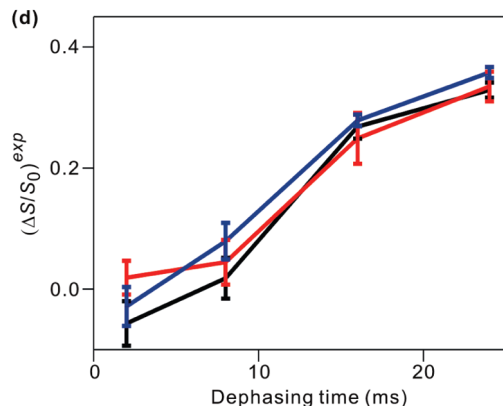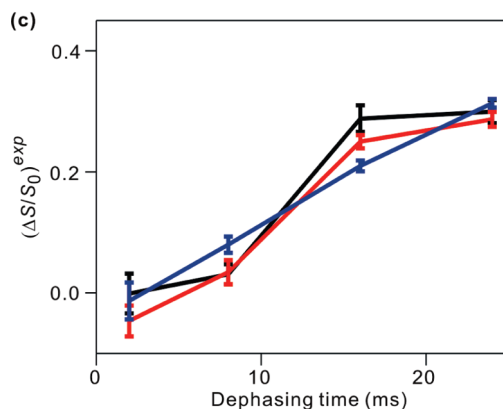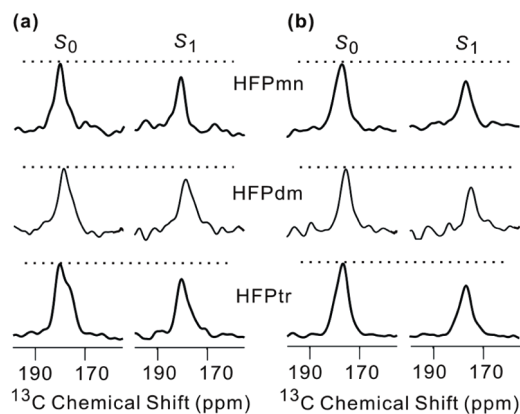
FIGURE 5: (a) $^{13}$C-detect/$^{31}$P-dephase REDOR $S_0$ and $S_1$ spectra for PC/PG membrane-associated HFPs and (b) spectra for PC/PG/CHOL membrane-associated HFPs. The samples for the top, middle, and bottom spectra contained HFPmn-A15, HFPdm-A15, and HFPtr-A15, respectively. Panels c and d display plots of $(\Delta S/S_0)^{exp}$ vs dephasing time with color coding: black for HFPmn, red for HFPdm, and blue for HFPtr. Experimental parameters and data presentation are very similar to those described in the legend of Figure 4. For panel a, the numbers of scans summed for each $S_0$ and $S_1$ spectrum were 41728 for HFPmn-A6, 68096 for HFPdm-A6, and 30720 for HFPtr-A6. For panel b, the numbers of scans were 28032 for HFPmn-A6, 82176 for HFPdm-A6, and 81536 for HFPtr-A6. In panel c, integration was centered at the peak chemical shift of the PC/PG samples (~178 ppm), and in panel d, integration was centered at the peak chemical shift of the PC/PG/CHOL samples (~176 ppm).

The $^{13}$CO chemical shift distributions in the $S_0$ spectra of Figures 4 and 5 provided information about local conformation with the analysis based on the literature conformational dependences of the $^{13}$CO shifts (*38*). For a single membrane composition, qualitatively similar NMR spectra and therefore conformational distributions were observed for the HFPmn,

Table 3: Best-Fit $^{13}C-^{31}P$ Dipolar Coupling ($d$) and Fractional Maximum Dephasing ($f$) Parameters for HFP-A15 Samples[a]

| | PC/PG | | | PC/PG/CHOL | | |
|---|---|---|---|---|---|---|
| | $d$ (Hz) | $f$ | $\chi^2$ | $d$ (Hz) | $f$ | $\chi^2$ |
| HFPmn-A15 | 75 (8) | 0.32 (0.02) | 8.0 | 88 (7) | 0.38 (0.03) | 6.7 |
| HFPdm-A15 | 62 (4) | 0.33 (0.02) | 6.8 | 72 (8) | 0.36 (0.03) | 3.5 |
| HFPtr-A15 | 90 (6) | 0.36 (0.01) | 0.3 | 90 (3) | 0.36 (0.01) | 1.9 |

[a] Fitting values are presented with uncertainties in parentheses. The $\chi^2$ values were calculated using eq S4 of the Supporting Information. The $d$ values in hertz are related to distances ($r$) in angstroms units using the relation $r = 23.05/d^{1/3}$. If $r = 5$ Å, $d = 98$ Hz, and if $r = 6$ Å, $d = 57$ Hz.

HFPdm, and HFPtr constructs. It was therefore unlikely that the large variations in lipid mixing rates among the constructs were due to conformational differences.

The $S_0$ spectra also provided specific information about the populations of helical and $\beta$ strand conformation at the Ala-6 and Ala-15 residues. There is a significant literature on the membrane-associated conformation of different HFP constructs with reports of both helical and $\beta$ strand conformations (2–5, 16, 22, 23). A higher HFP:lipid ratio is one factor which favors $\beta$ strand conformation and correlates with formation of $\beta$ sheet aggregates at higher peptide concentrations in the membrane (23). All of the NMR samples in this study had a peptide strand:lipid molar ratio of 0.04 but differed in the residue position of the labeled $^{13}CO$ group and in membrane cholesterol content. Consideration of membrane cholesterol may be important because cholesterol makes up ~30 mol % of host cell membranes and ~45 mol % of HIV membranes (34, 35).

The effect of membrane cholesterol on conformation is most clearly understood with the HFP-A6 $S_0$ spectra (cf. Figure 4a,b). In PC/PG membranes, the spectra exhibited a mixture of two signals with peak shifts of ~180 and ~175 ppm which were assigned to populations of helical and $\beta$ strand conformations, respectively (38). In PC/PG/CHOL membranes, there were single peaks with a shift of ~175 ppm, i.e., predominant $\beta$ strand conformation. Further evidence for correlation of the $\beta$ strand conformation with the 175 ppm shift is an earlier complete $^{13}C$ chemical shift assignment of residues 1–16 of HFPmn associated with cholesterol-containing membranes (24). The $^{13}C$ shifts of these residues, including Ala-6, were consistent with $\beta$ strand conformation.

For the HFP-A15 $S_0$ spectra, the effects of membrane cholesterol were more subtle (cf. Figure 5a,b). In PC/PG membranes, there was a dominant peak at ~178 ppm for all three constructs, and at least for HFPtr, there was also a clear shoulder at ~176 ppm. In PC/PG/CHOL membranes, there were single peaks at ~176 ppm. The 178 ppm signal was assigned to the helical conformation in part on the basis of the 181.2 and 179.1 ppm $^{13}CO$ shifts of Ala-6 and Ala-15, respectively, in detergent-associated HFPmn (17). These residues were helical in the detergent structure, and the 2 ppm difference in shifts correlated with the 2 ppm difference between the putative helical Ala-6 and Ala-15 shifts in PC/PG membranes. The 176 ppm shift in PC/PG/CHOL membranes was assigned to the $\beta$ strand conformation on the basis of (1) literature chemical shifts, (2) the previously described work on uniformly labeled HFPmn, and (3) earlier work showing specific antiparallel $\beta$ strand registries for a

large fraction of HFPmn in PC/PG/CHOL membranes (24, 38). In particular, this latter study demonstrated that an antiparallel $\beta$ sheet was formed for residues Ala-1–Gly-16 with an adjacent strand crossing near Phe-8 and Leu-9. For these registries, Ala-6 was in the middle and Ala-15 was near the edge of the $\beta$ sheets. The Ala-6 and Ala-15 residues would likely be in more and less ordered environments, respectively, which generally correlated with narrower ~3 ppm and broader 4–5 ppm line widths observed for these residues in PC/PG/CHOL membranes. Our interpretation of the HFP-A15 spectra was thus similar to that of the HFP-A6 spectra with helical and $\beta$ strand populations in PC/PG membranes and predominant $\beta$ strand conformation in PC/PG/CHOL membranes.

One overall conclusion of the chemical shift analysis was that membrane cholesterol was associated with the $\beta$ strand conformation of the HFP. Although this result had been previously suggested by work from our group, this study provides much clearer evidence of this observation because the only difference between the PC/PG and PC/PG/CHOL membranes was membrane cholesterol content. A similar correlation between membrane cholesterol and $\beta$ strand conformation has been observed for the influenza virus fusion peptide, so the correlation may be a general property of fusion peptides (41, 42). Although the reasons for the structural effect of membrane cholesterol are poorly understood, it is useful to consider the increased lateral molecular packing density in cholesterol-containing membranes and the difference in sizes of a putatively small monomeric HFP helix and a larger HFP $\beta$ sheet aggregate (43). Relative to the aggregate, the small helix might experience a more positive increase in free energy of membrane insertion with a higher packing density.

Spectra from other PC/PG samples with a peptide strand: lipid ratio of ≈0.04 (not shown) had populations of helical and $\beta$ strand chemical shifts that were similar to those displayed in Figure 4a. The general observations based on multiple samples were as follows. (1) The population of helical conformation was lower in HFPmn samples than in HFPdm and HFPtr samples (2) For all constructs, there was some $\beta$ strand population. The latter observation was consistent with earlier studies on HFPmn samples near this peptide strand:lipid ratio (23, 42). For HFPmn, HFPdm, and HFPtr samples with PC/PG/CHOL membranes, there was always predominant $\beta$ strand conformation (cf. Figure 4b). An earlier study showed that the $\beta$ strand conformation was also formed in samples made by the different protocol of initial cosolubilization of HFPmn, lipids, and cholesterol in organic solvent followed by removal of the solvent and then hydration (44). Therefore, the $\beta$ strand conformation in PC/PG/CHOL membranes is probably a thermodynamic equilibrium rather than a kinetically trapped structure.

For a particular construct, the lipid mixing rate was approximately independent of the absence or presence of membrane cholesterol (13). One interpretation of these data is that both the helical and $\beta$ strand HFP conformations induce vesicle fusion, while an alternate interpretation is that fusion is induced by unstructured HFP (45, 46). This transient HFP state would not be apparent in the NMR samples which reflect the long-time end-state HFP structure. Experimental support for the first interpretation is a HFPmn study which

showed that the rates of membrane binding and secondary structure formation were faster than the rate of lipid mixing (*47*).

As there were not large conformational variations among the HFPmn, HFPdm, and HFPtr constructs in a single membrane composition, HFP location in membranes was considered as a factor to explain the significant differences in fusion activities. In addition, detection of distinct signals for helical and $\beta$ strand $^{13}CO$ groups provided an opportunity to examine the dependence of membrane location on conformation. An earlier $^{13}CO-^{31}P$ REDOR study was carried out on HFPmn constructs containing $^{13}CO$ labels at three sequential residues (*30*). For HFPmn labeled from Ala-14 to Gly-16 in either PC/PG or PC/PG/CHOL membranes, $(\Delta S/S_0)^{exp} \approx 0.3-0.4$ with a dephasing time of 24 ms, while $(\Delta S/S_0)^{exp} \leq 0.15$ for HFPmn labeled from Gly-5 to Leu-7, from Phe-8 to Gly-10, or from Phe-11 to Gly-13. The overall conclusion was that the Ala-14−Gly-16 residues were closer to the lipid phosphate headgroups than were the Gly-5−Gly-13 residues. The singly $^{13}CO$ labeled samples of this study were consistent with these results and provided the following additional insights. (1) Ala-15 is closer to the phosphate headgroups than Ala-6 is. (2) This proximity difference is observed for both helical and $\beta$ strand conformations. (3) This difference is observed for the HFPmn, HFPdm, and HFPtr constructs. These insights are supported by the smaller $(\Delta S/S_0)^{exp}$ for all HFP-A6 constructs for both helical and $\beta$ strand conformations and the larger $(\Delta S/S_0)^{exp}$ for all HFP-A15 constructs for both helical and $\beta$ strand conformations (cf. Figures 4 and 5). The proximity of the Ala-15 residue to the phosphate groups may be an intrinsic property of the HFP sequence. This is perhaps explained by Ala-15 being at the junction of the more apolar N-terminal and the more polar C-terminal regions of the sequence. These regions likely have negative and positive free energies of membrane insertion, respectively (*48*). For signal-to-noise reasons, the experiments described in this paper were conducted at a nominal temperature of −50 °C in which the PC/PG membranes were in the gel phase and the PC/PG/CHOL membranes were in a glass of the liquid-ordered phase (*49*). Although we do not have data in the more biologically relevant higher-temperature liquid-crystalline and liquid-ordered phases, similar $^{13}CO-^{31}P$ REDOR studies have been carried out for the influenza virus fusion peptide in the lower-temperature gel and higher-temperature liquid-crystalline phases, and similar $(\Delta S/S_0)^{exp}$ values were obtained in both phases (*50*).

There is general consistency between our results and earlier experimental work on the location of HFPmn in membranes and micelles. Liquid-state NMR studies on helical HFPmn in detergent micelles showed that the Ala-15 residue was close to the detergent headgroups. In addition, the Ala-6 residue was in the micellar interior and farther from these headgroups (*17, 18*). The membrane location of HFPmn with a F8W mutation has been examined by fluorescence, and it was concluded that the Trp side chain was in the bilayer interior and was 10−11 Å from the phosphate group longitude. Very similar locations were found in samples with HFPmn-F8W:lipid ratios of 0.0025 and 0.02 and for membranes with or without cholesterol (*27, 28*). These data generally correlate with the small $(\Delta S/S_0)^{exp}$ of HFPmn-A6 in PC/PG and PC/PG/CHOL membranes.

Computer simulations have yielded two distinct models of the membrane location of helical HFPmn (*25, 26*). For the "deep insertion" model, there was traversal of both membrane leaflets, while in the "shallow insertion" model, HFPmn was restricted to the outer leaflet. For the deep insertion model, the Ala-6 and Ala-15 residues were ∼15 and ∼5 Å, respectively, from the phosphorus longitude, while in the shallow insertion model, they were ∼5 and ∼3 Å, respectively, from this longitude. Both models are consistent with the experimentally observed proximity of Ala-15 to the phosphate groups. However, the non-zero $(\Delta S/S_0)^{exp}$ values for the helical Ala-6 peak in HFPmn and HFPdm samples were not consistent with 100% deep insertion. There may be discrete populations of deeply and shallowly inserted helical HFPs (*21*).

Table 3 shows that the best-fit $d$ values for all HFP-A15 samples were consistent with 5−6 Å $^{13}CO-^{31}P$ distances. Qualitative consideration of these distances and the van der Waals radii of HFP and the phosphate group suggests close contact of the Ala-15 residue with the phosphate group. The fittings also resulted in best-fit $f$ values of 0.3−0.4 which were consistent with two populations of HFPs that differed in having Ala-15 close and far from the phosphate groups. For $\beta$ sheet structure, these populations could be strands at the edges and the middle of the sheet, respectively (*24*).

Although the data to date generally supported similar membrane locations of HFPmn, HFPdm, and HFPtr, there was some indication of differences in $(\Delta S/S_0)^{exp}$ for the helical peak in the HFP-A6 samples. In particular, Ala-6 appeared to be closest to the phosphate groups in HFPmn followed by HFPdm and HFPtr which would correlate with shallowest membrane insertion for HFPmn and deeper insertion for HFPdm and HFPtr. This suggests the intriguing hypothesis that the membrane insertion depth correlates with fusogenicity.

## ACKNOWLEDGMENT

## SUPPORTING INFORMATION AVAILABLE

Detailed description of NMR experiments, analysis and listing of values of $(\Delta S/S_0)^{exp}$, $(\Delta S/S_0)^{lab}$, and $(\Delta S/S_0)^{na}$ for the HFP-A15 samples, and detailed listing of the best-fit parameters for the lipid mixing data. This material is available free of charge via the Internet at http://pubs.acs.org.

## REFERENCES

1. Eckert, D. M., and Kim, P. S. (2001) Mechanisms of viral membrane fusion and its inhibition. *Annu. Rev. Biochem. 70*, 777–810.

2. White, J. M., Delos, S. E., Brecher, M., and Schornberg, K. (2008) Structures and mechanisms of viral membrane fusion proteins: Multiple variations on a common theme. *Crit. Rev. Biochem. Mol. Biol. 43*, 189–219.

3. Yang, J., Gabrys, C. M., and Weliky, D. P. (2001) Solid-state nuclear magnetic resonance evidence for an extended $\beta$ strand conformation of the membrane-bound HIV-1 fusion peptide. *Biochemistry 40*, 8126–8137.

4. Pereira, F. B., Goni, F. M., Muga, A., and Nieva, J. L. (1997) Permeabilization and fusion of uncharged lipid vesicles induced by the HIV-1 fusion peptide adopting an extended conformation: Dose and sequence effects. *Biophys. J. 73*, 1977–1986.

5. Durell, S. R., Martin, I., Ruysschaert, J. M., Shai, Y., and Blumenthal, R. (1997) What studies of fusion peptides tell us about viral envelope glycoprotein-mediated membrane fusion. *Mol. Membr. Biol. 14*, 97–112.

6. Pritsker, M., Rucker, J., Hoffman, T. L., Doms, R. W., and Shai, Y. (1999) Effect of nonpolar substitutions of the conserved Phe11 in the fusion peptide of HIV-1 gp41 on its function, structure, and organization in membranes. *Biochemistry 38*, 11359–11371.

7. Freed, E. O., Delwart, E. L., Buchschacher, G. L., Jr., and Panganiban, A. T. (1992) A mutation in the human immunodeficiency virus type 1 transmembrane glycoprotein gp41 dominantly interferes with fusion and infectivity. *Proc. Natl. Acad. Sci. U.S.A. 89*, 70–74.

8. Delahunty, M. D., Rhee, I., Freed, E. O., and Bonifacino, J. S. (1996) Mutational analysis of the fusion peptide of the human immunodeficiency virus type 1: Identification of critical glycine residues. *Virology 218*, 94–102.

9. Tan, K., Liu, J., Wang, J., Shen, S., and Lu, M. (1997) Atomic structure of a thermostable subdomain of HIV-1 gp41. *Proc. Natl. Acad. Sci. U.S.A. 94*, 12303–12308.

10. Weissenhorn, W., Dessen, A., Harrison, S. C., Skehel, J. J., and Wiley, D. C. (1997) Atomic structure of the ectodomain from HIV-1 gp41. *Nature 387*, 426–430.

11. Caffrey, M., Cai, M., Kaufman, J., Stahl, S. J., Wingfield, P. T., Covell, D. G., Gronenborn, A. M., and Clore, G. M. (1998) Three-dimensional solution structure of the 44 kDa ectodomain of SIV gp41. *EMBO J. 17*, 4572–4584.

12. Yang, R., Yang, J., and Weliky, D. P. (2003) Synthesis, enhanced fusogenicity, and solid state NMR measurements of cross-linked HIV-1 fusion peptides. *Biochemistry 42*, 3527–3535.

13. Yang, R., Prorok, M., Castellino, F. J., and Weliky, D. P. (2004) A trimeric HIV-1 fusion peptide construct which does not self-associate in aqueous solution and which has 15-fold higher membrane fusion rate. *J. Am. Chem. Soc. 126*, 14722–14723.

14. Zheng, Z., Yang, R., Bodner, M. L., and Weliky, D. P. (2006) Conformational flexibility and strand arrangements of the membrane-associated HIV fusion peptide trimer probed by solid-state NMR spectroscopy. *Biochemistry 45*, 12960–12975.

15. Farrera-Sinfreu, J., Royo, M., and Albericio, F. (2002) Undesired removal of the Fmoc group by the free ε-amino function of a lysine residue. *Tetrahedron Lett. 43*, 7813–7815.

16. Nieva, J. L., Nir, S., Muga, A., Goni, F. M., and Wilschut, J. (1994) Interaction of the HIV-1 fusion peptide with phospholipid vesicles: Different structural requirements for fusion and leakage. *Biochemistry 33*, 3201–3209.

17. Jaroniec, C. P., Kaufman, J. D., Stahl, S. J., Viard, M., Blumenthal, R., Wingfield, P. T., and Bax, A. (2005) Structure and dynamics of micelle-associated human immunodeficiency virus gp41 fusion domain. *Biochemistry 44*, 16167–16180.

18. Chang, D. K., Cheng, S. F., and Chien, W. J. (1997) The amino-terminal fusion domain peptide of human immunodeficiency virus type 1 gp41 inserts into the sodium dodecyl sulfate micelle primarily as a helix with a conserved glycine at the micelle-water interface. *J. Virol. 71*, 6593–6602.

19. Morris, K. F., Gao, X. F., and Wong, T. C. (2004) The interactions of the HIV gp41 fusion peptides with zwitterionic membrane mimics determined by NMR spectroscopy. *Biochim. Biophys. Acta 1667*, 67–81.

20. Li, Y. L., and Tamm, L. K. (2007) Structure and plasticity of the human immunodeficiency virus gp41 fusion domain in lipid micelles and bilayers. *Biophys. J. 93*, 876–885.

21. Gabrys, C. M., and Weliky, D. P. (2007) Chemical shift assignment and structural plasticity of a HIV fusion peptide derivative in dodecylphosphocholine micelles. *Biochim. Biophys. Acta 1768*, 3225–3234.

22. Epand, R. M. (2003) Fusion peptides and the mechanism of viral fusion. *Biochim. Biophys. Acta 1614*, 116–121.

23. Rafalski, M., Lear, J. D., and DeGrado, W. F. (1990) Phospholipid interactions of synthetic peptides representing the N-terminus of HIV gp41. *Biochemistry 29*, 7917–7922.

24. Qiang, W., Bodner, M. L., and Weliky, D. P. (2008) Solid-state NMR spectroscopy of human immunodeficiency virus fusion peptides associated with host-cell-like membranes: 2D correlation spectra and distance measurements support a fully extended conformation and models for specific antiparallel strand registries. *J. Am. Chem. Soc. 130*, 5459–5471.

25. Kamath, S., and Wong, T. C. (2002) Membrane structure of the human immunodeficiency virus gp41 fusion domain by molecular dynamics simulation. *Biophys. J. 83*, 135–143.

26. Maddox, M. W., and Longo, M. L. (2002) Conformational partitioning of the fusion peptide of HIV-1 gp41 and its structural analogs in bilayer membranes. *Biophys. J. 83*, 3088–3096.

27. Agirre, A., Flach, C., Goni, F. M., Mendelsohn, R., Valpuesta, J. M., Wu, F. J., and Nieva, J. L. (2000) Interactions of the HIV-1 fusion peptide with large unilamellar vesicles and monolayers. A cryo-TEM and spectroscopic study. *Biochim. Biophys. Acta 1467*, 153–164.

28. Haque, M. E., Koppaka, V., Axelsen, P. H., and Lentz, B. R. (2005) Properties and structures of the influenza and HIV fusion peptides on lipid membranes: Implications for a role in fusion. *Biophys. J. 89*, 3183–3194.

29. Gordon, L. M., Curtain, C. C., Zhong, Y. C., Kirkpatrick, A., Mobley, P. W., and Waring, A. J. (1992) The amino-terminal peptide of HIV-1 glycoprotein 41 interacts with human erythrocyte membranes: Peptide conformation, orientation and aggregation. *Biochim. Biophys. Acta 1139*, 257–274.

30. Qiang, W., Yang, J., and Weliky, D. P. (2007) Solid-state nuclear magnetic resonance measurements of HIV fusion peptide to lipid distances reveal the intimate contact of β strand peptide with membranes and the proximity of the Ala-14−Gly-16 region with lipid headgroups. *Biochemistry 46*, 4997–5008.

31. Lapatsanis, L., Milias, G., Froussios, K., and Kolovos, M. (1983) Synthesis of N-2,2,2-(trichloroethoxycarbonyl)-L-amino acids and N-(9-fluorenylmethoxycarbonyl)-L-amino acids involving succin-imidoxy anion as a leaving group in amino-acid protection. *Synthesis 8*, 671–673.

32. Kaiser, E., Colescott, R. L., Bossinger, C. D., and Cook, P. I. (1970) Color test for detection of free terminal amino groups in solid-phase synthesis of peptides. *Anal. Biochem. 34*, 595–598.

33. Struck, D. K., Hoekstra, D., and Pagano, R. E. (1981) Use of resonance energy transfer to monitor membrane fusion. *Biochemistry 20*, 4093–4099.

34. Aloia, R. C., Tian, H., and Jensen, F. C. (1993) Lipid composition and fluidity of the human immunodeficiency virus envelope and host cell plasma membranes. *Proc. Natl. Acad. Sci. U.S.A. 90*, 5181–5185.

35. Brugger, B., Glass, B., Haberkant, P., Leibrecht, I., Wieland, F. T., and Krasslich, H. G. (2006) The HIV lipidome: A raft with an unusual composition. *Proc. Natl. Acad. Sci. U.S.A. 103*, 2641–2646.

36. Yang, J., and Weliky, D. P. (2003) Solid state nuclear magnetic resonance evidence for parallel and antiparallel strand arrangements in the membrane-associated HIV-1 fusion peptide. *Biochemistry 42*, 11879–11890.

37. Toke, O., Maloy, W. L., Kim, S. J., Blazyk, J., and Schaefer, J. (2004) Secondary structure and lipid contact of a peptide antibiotic in phospholipid bilayers by REDOR. *Biophys. J. 87*, 662–674.

38. Zhang, H. Y., Neal, S., and Wishart, D. S. (2003) RefDB: A database of uniformly referenced protein chemical shifts. *J. Biomol. NMR 25*, 173–195.

39. Bak, M., Rasmussen, J. T., and Nielsen, N. C. (2000) SIMPSON: A general simulation program for solid-state NMR spectroscopy. *J. Magn. Reson. 147*, 296–330.

40. Balbach, J. J., Ishii, Y., Antzutkin, O. N., Leapman, R. D., Rizzo, N. W., Dyda, F., Reed, J., and Tycko, R. (2000) Amyloid fibril formation by Aβ$_{16-22}$, a seven-residue fragment of the Alzheimer's β-amyloid peptide, and structural characterization by solid state NMR. *Biochemistry 39*, 13748–13759.

41. Yang, J., Parkanzky, P. D., Bodner, M. L., Duskin, C. G., and Weliky, D. P. (2002) Application of REDOR subtraction for filtered MAS observation of labeled backbone carbons of membrane-bound fusion peptides. *J. Magn. Reson. 159*, 101–110.

42. Wasniewski, C. M., Parkanzky, P. D., Bodner, M. L., and Weliky, D. P. (2004) Solid-state nuclear magnetic resonance studies of HIV and influenza fusion peptide orientations in membrane bilayers using stacked glass plate samples. *Chem. Phys. Lipids 132*, 89–100.

43. Silvius, J. R. (2003) Role of cholesterol in lipid raft formation: Lessons from lipid model systems. *Biochim. Biophys. Acta 1610*, 174–183.

44. Yang, J., Prorok, M., Castellino, F. J., and Weliky, D. P. (2004) Oligomeric β structure of the membrane-bound HIV-1 fusion peptide formed from soluble monomers. *Biophys. J. 87*, 1951–1963.

45. Hofmann, M. W., Weise, K., Ollesch, J., Agrawal, P., Stalz, H., Stelzer, W., Hulsbergen, F., de Groot, H., Gerwert, K., Reed, J., and Langosch, D. (2004) De novo design of conformationally

flexible transmembrane peptides driving membrane fusion. *Proc. Natl. Acad. Sci. U.S.A. 101*, 14776–14781.

46. Reichert, J., Grasnick, D., Afonin, S., Buerck, J., Wadhwani, P., and Ulrich, A. S. (2007) A critical evaluation of the conformational requirements of fusogenic peptides in membranes. *Eur. Biophys. J. 36*, 405–413.

47. Buzon, V., Padros, E., and Cladera, J. (2005) Interaction of fusion peptides from HIV gp41 with membranes: A time-resolved membrane binding, lipid mixing, and structural study. *Biochemistry 44*, 13354–13364.

48. Hessa, T., Kim, H., Bihlmaier, K., Lundin, C., Boekel, J., Andersson, H., Nilsson, I., White, S. H., and Heijne, G. (2005) Recognition of tranmembrane helices by the endoplasmic reticulum translocon. *Nature 433*, 377–381.

49. Bloom, M., Evans, E., and Mouritsen, O. G. (1991) Physical properties of the fluid lipid-bilayer component of cell membranes: A perspective. *Q. Rev. Biophys. 24*, 293–397.

50. Sun, Y., and Weliky, D. P. Unpublished experiments.

Supporting Information for "The HIV Fusion Peptide and its Cross-Linked Oligomers: Efficient Syntheses, Significance of the Trimer in Fusion Activity, Correlation of β Strand Conformation with Membrane Cholesterol, and Proximity to Lipid Headgroups" by Wei Qiang and David P. Weliky

## 1. Solid-State NMR REDOR Experiments and Data Analysis

Experiments were done on a 9.4 T solid-state NMR spectrometer (Varian Infinity Plus, Palo Alto, CA) equipped with a triple resonance MAS probe. The detection channel was tuned to $^{13}$C at 100.8 MHz, the decoupling channel was tuned to $^{1}$H at 400.8 MHz, and the third channel was tuned to $^{31}$P at 162.2 MHz. The $^{13}$C shifts were externally referenced to the methylene resonance of adamantane at 40.5 ppm, $^{31}$P shifts were referenced to 85% $H_3PO_4$ at 0 ppm, and the $^{13}$C and $^{31}$P transmitter chemical shifts were 156 and –16 ppm, respectively. The $^{13}$C referencing allows direct comparison with $^{13}$C shift databases derived from liquid-state NMR assignments of proteins (*1-3*). Samples were cooled with nitrogen gas at –50 $^{o}$C to enhance signal and to prevent motional averaging of the dipolar coupling. The HFP chemical shifts and presumably HFP conformation are very similar in cooled and ambient temperature samples (*4*). The MAS frequency was 8000 ± 2 Hz, and the recycle delay was 1 s.

The sample used for calibration of the REDOR parameters contained 0.8 μmol unlabeled HFPmn and 20 μmol 1,2-dipalmitoyl[1-$^{13}$C]-*sn*-glycero-3-phosphocholine (DPPC-$^{13}$C). The sample was prepared according to the protocol of the main text, the $^{13}$CO signal was dominated by the labeled nuclei, and the $^{13}$CO-$^{31}$P distances were 5 – 6 Å (*5*). The $^{1}$H and $^{13}$C rf fields were initially calibrated with adamantane and the $^{13}$C

1

cross-polarization field was then adjusted to give the maximum $^{13}CO$ signal of the standard sample. The $^{31}P$ $\pi$ pulse length was set by minimization of the $S_1$ signal in this sample for $\tau = 24$ ms and the $^1H$ TPPM pulse length was set to give the maximum $S_0$ signal. The parameter values were confirmed by determination of $d$ from analysis of REDOR data in the sample for $\tau$ between 1 and 19 ms. The best-fit $d = 68$ Hz corresponded to the reasonable value $r = 5.6$ Å (6).

Each spectrum was processed with 300 Hz Gaussian line broadening and polynomial baseline correction. Integration of the $^{13}CO$ peak over a 1 ppm range in the $S_0$ and $S_1$ spectra yielded integrals which were denoted "$S_0^{exp}$" and "$S_1^{exp}$", respectively. The dipolar coupling was assessed from variation of the normalized experimental dephasing parameter $(\Delta S/S_0)^{exp}$ with $\tau$ where $(\Delta S/S_0)^{exp} = 1 - S_1^{exp}/S_0^{exp}$. The uncertainty in $(\Delta S/S_0)^{exp}$, $\sigma^{exp}$, was determined from $\sigma_{S_0}$, the root-mean-squared deviation of twelve integration regions (1 ppm) in the $S_0$ spectrum, and from the analogous quantity $\sigma_{S_1}$ (7):

$$\sigma^{exp} = \frac{\sqrt{\left[\left(S_0^{exp}\right)^2 \times \sigma_{S_1}^2\right] + \left[\left(S_1^{exp}\right)^2 \times \sigma_{S_0}^2\right]}}{\left(S_0^{exp}\right)^2} \qquad \text{(Eq. S1)}$$

The labeled HFP $^{13}CO$ nucleus provided the dominant (~75%) contribution to $S_0^{exp}$ and $S_1^{exp}$ and a plot of $(\Delta S/S_0)^{exp}$ vs $\tau$ provided qualitative and semi-quantitative information about the proximity of this $^{13}CO$ nucleus to the $^{31}P$ nuclei in the membrane. The HFPmn-A15, HFPdm-A15, and HFPtr-A15 samples had large $(\Delta S/S_0)^{exp}$ and more quantitative analysis was made for the dipolar coupling between the labeled $^{13}CO$ nucleus and the closest $^{31}P$ nucleus. The analysis considered that $S_0^{exp}$ had labeled ($S_0^{lab}$) and natural abundance ($S_0^{na}$) contributions and that $S_1^{exp}$ had analogous contributions. The

resultant $(\Delta S/S_0)^{lab}$ were directly compared to $(\Delta S/S_0)^{sim}$ calculated for dipolar coupling of

a single $^{13}\text{CO}$-$^{31}\text{P}$ spin pair:

$$\left(\frac{\Delta S}{S_0}\right)^{lab} \approx \left[\left(1 + \frac{S_0^{na}}{S_0^{lab}}\right) \times \left(\frac{\Delta S}{S_0}\right)^{exp}\right] - \left[\left(\frac{S_0^{na}}{S_0^{lab}}\right) \times \left(\frac{\Delta S}{S_0}\right)^{na}\right] \qquad \text{(Eq. S2)}$$

The $S_0^{na}\big/S_0^{lab} = 0.32$ and was calculated as (fractional $^{13}\text{C}$ natural abundance) × (total

number of residues – number of labeled residues)/(number of labeled residues).

Calculations of $(\Delta S/S_0)^{na}$ were based on previously determined $(\Delta S/S_0)^{exp}$ for membrane-

associated HFPmn samples which were triply $^{13}\text{CO}$ labeled at three residues: Ala-1 to

Val-3, Gly-5 to Leu-7, Phe-8 to Gly-10, Phe-11 to Gly-13, or Ala-14 to Gly-16 (*6*). For a

particular membrane composition and value of $\tau$, the $(\Delta S/S_0)^{na}$ was calculated as the

average of the corresponding $(\Delta S/S_0)^{exp}$ of the triply labeled samples. In PC:PG

membranes, $(\Delta S/S_0)^{na} = 0.024, 0.077, 0.143$ and $0.197$ for $\tau = 2, 8, 16$ and 24 ms,

respectively, and in PC:PG:CHOL membranes, $(\Delta S/S_0)^{na} = 0.028, 0.051, 0.122$ and $0.145$

for $\tau = 2, 8, 16$ and 24 ms, respectively. The ratios $(\Delta S/S_0)^{lab}/(\Delta S/S_0)^{exp}$ typically varied

between 0.9 and 1.2 and the $(\Delta S/S_0)^{lab}$ were not strongly dependent on the value of

$(\Delta S/S_0)^{na}$. Further derivation and details are provided in Section 2.

The $\sigma^{lab}$ were calculated with $\sigma^{lab} = (1 + S_0^{na}/S_0^{lab}) \times \sigma^{exp}$ which neglected the

small contribution from the far-right term in Eq. S2. Simulations of the experimental data

were based on a single $^{13}\text{CO}$-$^{31}\text{P}$ spin pair model:

$$\left(\frac{\Delta S}{S_0}\right)^{sim} = 1 - [J_0(\sqrt{2}\lambda)]^2 + \left\{2 \times \sum_{k=1}^{5} \frac{[J_k(\sqrt{2}\lambda)]^2}{16k^2 - 1}\right\} \qquad \text{(Eq. S3)}$$

with $\lambda = d \times \tau$ and $J_k$ as the $k^{th}$ order Bessel function of the first kind ($8$). The samples

contained multiple $^{13}CO$-$^{31}P$ distances and couplings and these are approximated as a

single $d$ and a single $r$ in Eq. S3 ($9$-$12$).

At larger $\tau$, the $(\Delta S/S_0)^{exp}$ and the $(\Delta S/S_0)^{lab}$ reached plateau values which were

significantly smaller than 1 while the $(\Delta S/S_0)^{sim}$ had plateau values of ~1. This

inconsistency was resolved using a model of two populations of membrane-associated

HFPs. The "$f$" fraction represented the HFPs whose Ala-15 $^{13}COs$ were close to the lipid

$^{31}Ps$ with corresponding $d \neq 0$ while the "$1-f$" fraction represented the HFPs whose Ala-

15 $^{13}COs$ were far from the lipid $^{31}Ps$ with corresponding $d = 0$. Fitting was done with an

array of values of $d$ and $f$ and the best-fit $d$ corresponded to the minimum

$\chi^2(d,f)$:

$$\chi^2(d,f) = \sum_{i=1}^{T} \frac{\left[ \left(\frac{\Delta S}{S_0}\right)_i^{lab} - \left\{ f \times \left(\frac{\Delta S}{S_0}(d)\right)_i^{sim} \right\} \right]^2}{(\sigma_i^{lab})^2} \qquad \text{(Eq. S4)}$$

where $T$ is the number of $\tau$ values. The uncertainties of $d$ and $f$ were calculated with the

$\chi^2 = \chi^2_{min} + 1$ criterion ($7$).

## 2. $(\Delta S/S_0)^{exp}$, $(\Delta S/S_0)^{lab}$, and $(\Delta S/S_0)^{na}$ for the HFP-A15 Samples

The definition of $(\Delta S/S_0)^{exp}$:

$$\left(\frac{\Delta S}{S_0}\right)^{exp} = \frac{S_0^{lab} + S_0^{na} - S_1^{lab} - S_1^{na}}{S_0^{lab} + S_0^{na}} = 1 - \frac{S_1^{lab}}{S_0^{lab} + S_0^{na}} - \frac{S_1^{na}}{S_0^{lab} + S_0^{na}} \qquad \text{(Eq. S5)}$$

where $exp \equiv$ experimental, $lab \equiv$ labeled, and $na \equiv$ natural abundance. Multiplication of

the left-most and right-most sides of Eq. S5 by $(S_0^{lab} + S_0^{na})/S_0^{lab}$ is followed by algebraic

manipulation:

$$\left[\left(1 + \frac{S_0^{na}}{S_0^{lab}}\right) \times \left(\frac{\Delta S}{S_0}\right)^{exp}\right] = \left(\frac{\Delta S}{S_0}\right)^{lab} + \frac{\left(\Delta S^{na}\right)}{S_0^{lab}} \quad \text{(Eq. S6)}$$

Multiplication of the right-most term by $(S_0^{na}/S_0^{na})$ is followed by algebraic manipulation to yield Eq. S2:

$$\left(\frac{\Delta S}{S_0}\right)^{lab} = \left[\left(1 + \frac{S_0^{na}}{S_0^{lab}}\right) \times \left(\frac{\Delta S}{S_0}\right)^{exp}\right] - \left[\left(\frac{S_0^{na}}{S_0^{lab}}\right) \times \left(\frac{\Delta S}{S_0}\right)^{na}\right]$$

$$= \left[1.32 \times \left(\frac{\Delta S}{S_0}\right)^{exp}\right] - \left[0.32 \times \left(\frac{\Delta S}{S_0}\right)^{na}\right] \quad \text{(Eq. S7)}$$

where $S_0^{na}/S_0^{lab} = 0.32$ was determined using the $^{13}C$ natural abundance (0.011) and the

~1:29 ratio of labeled to unlabeled amino acids in each sample. The values of $(\Delta S/S_0)^{na}$

were calculated using the average of the $(\Delta S/S_0)^{exp}$ values determined for HFPmn samples

which were $^{13}CO$ labeled at three sequential residues, cf. Tables S1 and S2.

**Table S1**. $(\Delta S/S_0)^{exp}$ as a function of dephasing time in PC:PG membranes [a,b,c]

| Dephasing time (ms) | Peptide | | | | |
|---|---|---|---|---|---|
| | HFPmn-[1]AVG | HFPmn-[5]GAL | HFPmn-[8]FLG | HFPmn-[11]FLG | HFPmn-[14]AAG |
| 2 | 0.046 | 0.002 | -0.030 | 0.030 | 0.002 |
| 8 | 0.052 | 0.080 | -0.032 | 0.035 | 0.210 |
| 16 | 0.134 | 0.076 | 0.077 | 0.105 | 0.374 |
| 24 | 0.248 | 0.145 | 0.100 | 0.143 | 0.415 |

**Table S2**. $(\Delta S/S_0)^{exp}$ as a function of dephasing time in PC:PG:CHOL membranes [a,b,c]

| Dephasing time (ms) | Peptide | | | | |
|---|---|---|---|---|---|
| | HFPmn-[1]AVG | HFPmn-[5]GAL | HFPmn-[8]FLG | HFPmn-[11]FLG | HFPmn-[14]AAG |
| 2 | 0.048 | 0.012 | 0.025 | 0.038 | 0.013 |
| 8 | 0.049 | 0.047 | -0.010 | 0.040 | 0.151 |
| 16 | 0.136 | 0.073 | 0.054 | 0.089 | 0.270 |
| 24 | 0.205 | 0.052 | 0.035 | 0.163 | 0.312 |

[a] "HFPmn–[1]AVG" was $^{13}$CO labeled at Ala-1, Val-2, and Gly-3, "HFPmn–[5]GAL" was $^{13}$CO labeled at Gly-5, Ala-6, and Leu-7, etc.
[b] Data for the HFPmn-[1]AVG sample are from the present study while data for other samples are from earlier studies (*6*).
[c] The typical uncertainty in each $(\Delta S/S_0)^{exp}$ value is ±0.01.

For each membrane composition and each $\tau$:

$$\left(\frac{\Delta S}{S_0}\right)^{na} = \frac{\left(\frac{\Delta S}{S_0}\right)^{exp}_{HFPmn-^1AVG} + \left(\frac{\Delta S}{S_0}\right)^{exp}_{HFPmn-^5GAL} + \left(\frac{\Delta S}{S_0}\right)^{exp}_{HFPmn-^8FLG} + \left(\frac{\Delta S}{S_0}\right)^{exp}_{HFPmn-^{11}FLG} + \left(\frac{\Delta S}{S_0}\right)^{exp}_{HFPmn-^{14}AAG}}{5}$$

(Eq. S8)

**Table S3**. $(\Delta S/S_0)^{na}$ values calculated using Eq. S8

| Dephasing time (ms) | PC:PG membranes | PC:PG:CHOL membranes |
|---|---|---|
| 2 | 0.024 | 0.028 |
| 8 | 0.077 | 0.051 |
| 16 | 0.143 | 0.122 |
| 24 | 0.197 | 0.145 |

**Table S4**. $(\Delta S/S_0)^{exp}$ and $(\Delta S/S_0)^{lab}$ for HFP-A15/PC:PG samples [a,b]

| Dephasing time (ms) | HFPmn | | HFPdm | | HFPtr | |
|---|---|---|---|---|---|---|
| | $(\Delta S/S_0)^{exp}$ | $(\Delta S/S_0)^{lab}$ | $(\Delta S/S_0)^{exp}$ | $(\Delta S/S_0)^{lab}$ | $(\Delta S/S_0)^{exp}$ | $(\Delta S/S_0)^{lab}$ |
| 2 | 0.00(7) | 0.00(9) | -0.05(5) | -0.07(7) | -0.01(7) | -0.03(8) |
| 8 | 0.03(3) | 0.01(4) | 0.03(4) | 0.02(5) | 0.08(3) | 0.08(4) |
| 16 | 0.29(4) | 0.33(6) | 0.25(2) | 0.28(3) | 0.21(2) | 0.23(2) |
| 24 | 0.30(4) | 0.33(5) | 0.29(3) | 0.31(3) | 0.31(1) | 0.35(2) |

**Table S5**. $(\Delta S/S_0)^{exp}$ and $(\Delta S/S_0)^{lab}$ for HFP-A15/PC:PG:CHOL samples [a,b]

| Dephasing time (ms) | HFPmn | | HFPdm | | HFPtr | |
|---|---|---|---|---|---|---|
| | $(\Delta S/S_0)^{exp}$ | $(\Delta S/S_0)^{lab}$ | $(\Delta S/S_0)^{exp}$ | $(\Delta S/S_0)^{lab}$ | $(\Delta S/S_0)^{exp}$ | $(\Delta S/S_0)^{lab}$ |
| 2 | -0.06(7) | -0.08(9) | 0.02(6) | 0.02(8) | -0.03(6) | -0.05(8) |
| 8 | 0.02(7) | 0.00(9) | 0.04(8) | 0.04(10) | 0.08(6) | 0.09(8) |
| 16 | 0.27(4) | 0.31(5) | 0.25(8) | 0.29(11) | 0.28(2) | 0.32(3) |
| 24 | 0.33(3) | 0.38(3) | 0.34(5) | 0.39(7) | 0.36(2) | 0.42(2) |

[a] Uncertainties are given in parentheses.
[b] The $(\Delta S/S_0)^{exp}$ values were determined from $S_0$ and $S_1$ integrals that had 1 ppm width and that were centered around 178 ppm (Table S4) or 176 ppm (Table S5).

The ratios $(\Delta S/S_0)^{lab}/(\Delta S/S_0)^{exp}$ typically varied between 0.9 and 1.2 and the $(\Delta S/S_0)^{lab}$ were not strongly dependent on the value of $(\Delta S/S_0)^{na}$.

**Figure S1**. Plot of $(\Delta S/S_0)^{lab}$ (lines showing error bars) and the best-fit $(\Delta S/S_0)^{sim}$ (circles) vs dephasing time for the HFPtr-A15/PC:PG sample. The best-fit $d$ and $f$ used to calculate $(\Delta S/S_0)^{sim}$ are listed in Table 3 in the main text and were calculated using Eq S4.
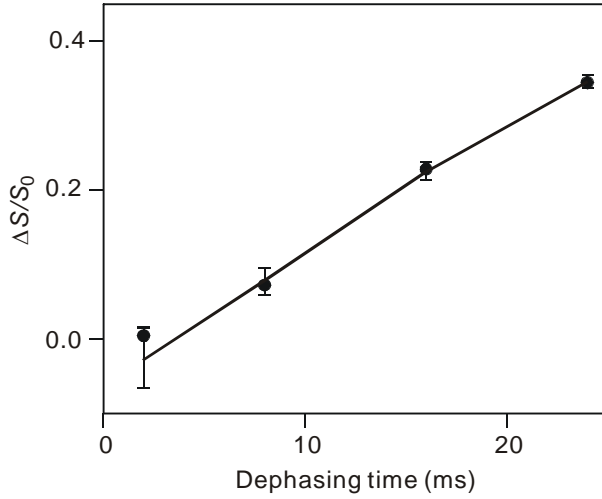


## 3. Fitting of the Lipid Mixing Data

Table 2 in the main text lists the best-fit parameters for the normalized fluorescence data $F(t)$ vs $t$ at 35 °C. Fitting at other temperatures was also done using Eq. 2 in the main text which is reproduced here for clarity.

$$F(t) = F_0 + F_1(1 - e^{-k_1 t}) + F_2(1 - e^{-k_2 t}) \qquad \text{(Eq. S9)}$$

**Table S6**. Best-fit parameters for HFPdm [a]

| Temp. (ºC) | $k_1 (10^{-3}\,s^{-1})$ | $k_2 (10^{-3}\,s^{-1})$ | $F_0$ (a.u.) | $F_1$ (a.u.) | $F_2$ (a.u.) |
|---|---|---|---|---|---|
| 25 | 32.0(0.4) | 3.5(0.4) | 0.4(0.1) | 18.9(1.1) | 19.6(1.4) |
| 30 | 42.0(0.4) | 3.9(0.3) | 0.3(0.1) | 19.7(0.7) | 19.5(0.6) |
| 35 | 54.9(0.3) | 4.9(0.2) | 0.5(0.1) | 19.6(0.3) | 19.8(0.1) |
| 40 | 69.9(0.5) | 6.5(0.2) | 0.7(0.1) | 19.7(0.3) | 19.8(0.3) |

**Table S7**. Best-fit parameters for HFPtr [a]

| Temp. (ºC) | $k_1 (10^{-3}\,s^{-1})$ | $k_2 (10^{-3}\,s^{-1})$ | $F_0$ (a.u.) | $F_1$ (a.u.) | $F_2$ (a.u.) |
|---|---|---|---|---|---|
| 25 | 95.2(0.9) | 11.6(0.1) | 0.4(0.1) | 50.1(1.1) | 50.0(0.7) |
| 30 | 116.3(2.7) | 14.3(0.2) | 0.7(0.1) | 50.0(1.5) | 49.9(1.1) |
| 35 | 139(3) | 17.3(0.3) | 0.9(0.2) | 50.1(0.2) | 50.0(0.2) |
| 40 | 156.2(4.7) | 19.3(0.2) | 0.9(0.2) | 50.1(0.8) | 49.9(0.7) |

**Table S8**. Best-fit parameters for HFPte [a]

| Temp. (ºC) | $k_1 (10^{-3}\,s^{-1})$ | $k_2 (10^{-3}\,s^{-1})$ | $F_0$ (a.u.) | $F_1$ (a.u.) | $F_2$ (a.u.) |
|---|---|---|---|---|---|
| 25 | 141(6) | 12.4(0.1) | 0.6(0.2) | 50.0(0.7) | 50.1(0.5) |
| 30 | 164(6) | 14.5(0.2) | 0.6(0.3) | 50.1(0.7) | 50.0(0.4) |
| 35 | 185(7) | 20.7(0.3) | 0.9(0.3) | 49.8(0.3) | 50.1(0.2) |
| 40 | 208(8) | 20.7(0.1) | 1.1(0.3) | 50.0(0.6) | 50.0(0.5) |

[a] Uncertainties are given in parentheses.

**Figure S2**. Plots of the normalized fluorescence $F(t)$ (squares) and best-fitting (red curve) vs time for HFPte at 25ºC.
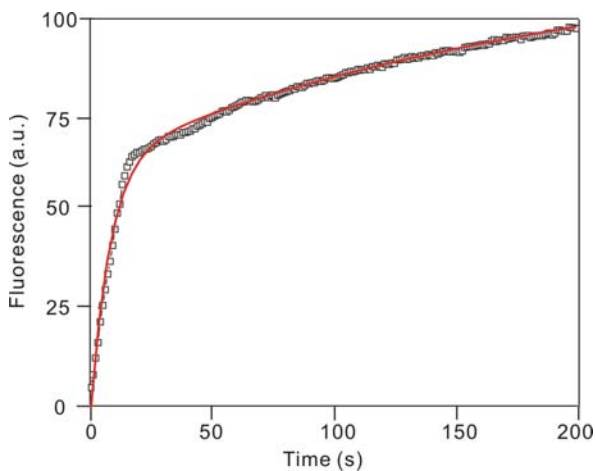
## 4.    References

(1)     Zhang, H. Y., Neal, S., and Wishart, D. S. (2003) RefDB: A database of uniformly referenced protein chemical shifts. *J. Biomol. NMR 25*, 173-195.

(2)     Morcombe, C. R., and Zilm, K. W. (2003) Chemical shift referencing in MAS solid state NMR. *J. Magn. Reson. 162*, 479-486.

(3)     Igumenova, T. I., McDermott, A. E., Zilm, K. W., Martin, R. W., Paulson, E. K., and Wand, A. J. (2004) Assignments of carbon NMR resonances for microcrystalline ubiquitin. *J. Am. Chem. Soc. 126*, 6720-6727.

(4)     Bodner, M. L., Gabrys, C. M., Parkanzky, P. D., Yang, J., Duskin, C. A., and Weliky, D. P. (2004) Temperature dependence and resonance assignment of $^{13}$C NMR spectra of selectively and uniformly labeled fusion peptides associated with membranes. *Magn. Reson. Chem. 42*, 187-194.

(5)     Venable, R. M., Brooks, B. R., and Pastor, R. W. (2000) Molecular dynamics simulations of gel (L$_{\beta I}$) phase lipid bilayers in constant pressure and constant surface area ensembles. *J. Chem. Phys. 112*, 4822-4832.

(6)     Qiang, W., Yang, J., and Weliky, D. P. (2007) Solid-state nuclear magnetic resonance measurements of HIV fusion peptide to lipid distances reveal the intimate contact of beta strand peptide with membranes and the proximity of the Ala-14-Gly-16 region with lipid headgroups. *Biochemistry 46*, 4997-5008.

(7)     Bevington, P. R., and Robinson, D. K. (1992) *Data Reduction and Error Analysis for the Physical Sciences*, 2nd ed., McGraw-Hill, Boston.

(8)     Mueller, K. T. (1995) Analytical solutions for the time evolution of dipolar-dephasing NMR signals. *J. Magn. Reson. Ser. A 113*, 81-93.

(9)     Yang, J., and Weliky, D. P. (2003) Solid state nuclear magnetic resonance evidence for parallel and antiparallel strand arrangements in the membrane-associated HIV-1 fusion peptide. *Biochemistry 42*, 11879-11890.

(10)    Toke, O., Maloy, W. L., Kim, S. J., Blazyk, J., and Schaefer, J. (2004) Secondary structure and lipid contact of a peptide antibiotic in phospholipid bilayers by REDOR. *Biophys. J. 87*, 662-674.

(11)   Raghunathan, V., Gibson, J. M., Goobes, G., Popham, J. M., Louie, E. A., Stayton, P. S., and Drobny, G. P. (2006) Homonuclear and heteronuclear NMR studies of a statherin fragment bound to hydroxyapatite crystals. *J. Phys. Chem. B 110*, 9324-9332.

(12)    Doherty, T., Waring, A., and Hong, M. (2006) Membrane-bound conformation and topology of the antimicrobial peptide tachyplesin I by solid-state NMR. *Biochemistry 45*, 13323-13330.